Topology optimization for 3D fluid diode design considering wall-connected structures

Takamitsu Sasaki, Kozo Furuta, Naoyuki Ishida, Hao Li, Tsuguo Kondoh, Kazuhiro Izui, Shinji Nishiwaki

Topology optimization for 3D fluid diode design considering wall-connected structures

Takamitsu Sasaki[1*], Kozo Furuta[2†], Naoyuki Ishida[1†], Hao Li[1†], Tsuguo Kondoh[1†], Kazuhiro Izui[2†], Shinji Nishiwaki[1†]

[1*]Department of Mechanical Engineering and Science, Kyoto University, Kyoto Daigaku Katsura, Nishikyo-ku, Kyoto, 615-8530, Japan.
[2]Department of Micro Engineering, Kyoto University, Kyoto Daigaku Katsura, Nishikyo-ku, Kyoto, 615-8530, Japan.

*Corresponding author(s). E-mail(s): sasaki.takamitsu.36c@st.kyoto-u.ac.jp;
†These authors contributed equally to this work.

Abstract

This paper proposes a density-based topology optimization method for the three-dimensional design of fluid diodes considering wall-connected structures based on the fictitious physical modelling approach. The optimum design problem of fluid diodes is formulated as maximizing the energy dissipation in the reverse flow subject to the upper bound constraint of the energy dissipation in the forward flow. A fictitious physical model and a geometric constraint are constructed to detect and restrict the "floating" solid domains, which are not connected to the outer boundaries. The sensitivities of cost functions are derived and computed based on the continuous adjoint method. The finite volume method is employed to discretize the governing and adjoint equations to mitigate the huge computational costs of three-dimensional fluid analysis. Numerical investigations are presented to validate the fictitious physical model and the geometric constraint for excluding "floating" islands. Finally, topology optimization for fluid diodes with and without the geometric constraint is performed, and the result demonstrates that the proposed method is capable of generating fluid diodes with wall connectivity while maintaining a good functional performance.

Keywords: Topology optimization, Fluid diodes design, Wall-connected structures, Geometric constraint, Finite volume method

1 Introduction

Fixed-geometry fluid diodes or no-moving-part valves (e.g. Tesla valves) are check valves without moving parts or deformation whose resistance depends on flow directions. The geometry of fluid diodes is designed so that the fluid can flow with little resistance in the forward direction while fluidic inertial forces generate huge resistance in the reverse direction. Since fluid diodes without any moving parts are easy to fabricate and resistant to wear and fatigue, they are widely used as components of micropumps [Forster et al., 1995, Morganti et al., 2005, Nabavi, 2009].

A number of studies have been conducted to improve the performance of fluid diodes. Most of the previous studies have employed a measure of diodicity, defined as the ratio of the pressure drop in the reverse flow to that in the forward flow,

as a measure of the performance of fluid diodes. Truong and Nguyen [2003] investigated the design optimization parameters for fluid diodes such as the length and the cross angle of channels and conducted a parametric optimization. Gamboa et al. [2005] applied shape optimization and obtained the geometry with significantly improved diodicity over the Reynolds number $0 < \mathrm{Re} \leq 2000$. Although these studies have achieved improvements in fluid diode performance, the topology of target geometry does not change during the optimization process in these methods.

Topology optimization has advantages over those optimization methods in that the topology of the structure can be changed during the optimization process, leading to a significant performance improvement. In this method, the structural optimization problem is replaced with a material distribution problem, and optimal distribution is obtained based on mathematical and physical principles. Topology optimization originated in solid mechanics [Bendsøe and Kikuchi, 1988] and has since been extended to other physical phenomena. The pioneer work of topology optimization in fluid problems was done by Borrvall and Petersson [2003], in which Stokes equations were considered with a density-based method introducing Darcy law (also called the Brinkman model). Based on this approach, topology optimization has been extended to Navier-Stokes equations [Gersborg-Hansen et al., 2005, Olesen et al., 2006, Zhou and Li, 2008], non-Newtonian [Pingen and Maute, 2010], unsteady [Kreissl et al., 2011, Deng et al., 2011], and turbulent flows [Kontoleontos et al., 2013, Yoon, 2016, Dilgen et al., 2018], and applied to a variety of design problems, e.g., optimum design of rotor machines [Romero and Silva, 2014], aerodynamics [Li et al., 2022b, Ghasemi and Elham, 2022], heat sinks [Yaji et al., 2015, Li et al., 2022a] in three dimensions.

Topology optimization was also applied to design problems of fluid diodes [Deng et al., 2010, Lin et al., 2015]. Lin et al. [2015] formulated the optimal design problem for fluid diodes as maximizing diodicity subject to a volume constraint with an additional penalty on flow through intermediate density. Sato et al. [2017a] proposed a bi-objective topology optimization method for fluid diodes and investigated Pareto-optimal solutions. In work done by Guo et al. [2020], length scale constraints were introduced into two-dimensional topology optimization for the design of fluid diodes to reduce the difference between the performance of the two-dimensional model and the three-dimensional model obtained from the extrusion.

Although these previous studies showed that topology optimization can generate novel designs of fluid diodes with improved performances, one limitation in the design problems is the two-dimensional assumption of fluid flow. This assumption is valid as long as the effect of upper and lower boundaries is negligible. In practice, however, the height of the flow channel is not infinite, and the discrepancy between the performances of the two-dimensional model and the extruded three-dimensional model should not be neglected. Lin et al. [2015] reported that the diodicity values of the extruded three-dimensional model of fluid diodes measured by both numerical simulations and experiments were less than those of the two-dimensional model, and they concluded that topology optimization in three dimensions should be performed when the height of the channel cannot be neglected. Although Guo et al. [2020] showed that length scale control can mitigate the discrepancy, difficulty in estimating the final performance still remains. Thus, this work sheds a light on the topology optimization of fluid diodes in full-scale three-dimensional setting.

However, topology optimization of fluid diodes in three dimensions poses another challenging issue. The optimized structures may feature some "floating" islands disconnected to the external walls, which is not ideal in practice, therefore, cannot be manufactured. The Brinkman model allows the nucleation of such structures owing to the nature of its mathematical modelling. Therefore, we need to construct a design methodology for obtaining wall-connected structures in the fluid topology optimization.

Previous works have investigated geometric constraints for ensuring desired geometrical features of the structure, especially in the fields of solid mechanics and additive manufacturing. In topology optimization, the control of minimum and maximum length scales of structures has long been a typical issue of geometric constraints [Poulsen, 2003, Guest et al., 2004, Zhou et al., 2015, Guest, 2009, Li et al., 2023], and the concept of geometric constraints have been

extended to molding constraints [Xia et al., 2010, Allaire et al., 2016, Sato et al., 2017b] and enclosed voids restriction constraints [Liu et al., 2015, Li et al., 2016, Yamada and Noguchi, 2022]. In the work of Liu et al. [2015], a Virtual Temperature Method (VTM) was constructed, in which a virtual boundary value problem is introduced so that the enclosed void regions can appear with a high value of virtual temperature. The fictitious physical model to constrain closed cavities proposed by Yamada and Noguchi [2022] is similar to VTM in concept, but the governing equations for the fictitious physical field are different. Both of these methods successfully obtained optimal structures in which enclosed void regions do not exist, and all void regions have connections to the outer boundaries. We can impose a geometric constraint for ensuring wall-connected structures of the fluid diodes by considering the enclosed void regions in these methods as floating solid regions.

This paper proposes a topology optimization of fluid diodes considering wall-connected structures. Since excessive energy dissipation in the forward flow impairs the original function as a flow path, the optimal design problem of fluid diodes is formulated as maximizing the energy dissipation in the reverse flow subject to a maximum allowed energy dissipation in the forward flow. An additional geometric constraint based on the fictitious physical approach is formulated to avoid the nucleation of "floating" islands in the optimum design problem. To the authors' best knowledge, very limited works have been proposed to guarantee wall-connected structures in the three-dimensional fluid topology optimization. In numerical implementation, to overcome the problems of numerical costs of three-dimensional fluid flow analysis, every implementation is performed in OpenFOAM, an open-source finite volume software which is widely used in computational fluid dynamics and topology optimization related to fluid problems [Yu et al., 2020, Pan et al., 2022, Galanos et al., 2022].

The remainder of this paper is organized as follows. In Section 2, the governing equations and density-based topology optimization formulation of incompressible steady-state flow are described, and the fictitious physical field and the geometric constraint are introduced. Then, the optimal design problem of fluid diodes considering wall-connected structures is defined. In Section 3, we describe the implementation details and the optimization algorithm. In Section 4, we show a numerical verification of the fictitious physical model and design examples of fluid diodes obtained from the proposed method. Finally, conclusions are provided in Section 5.

2 Formulation

2.1 Governing equations

The governing equations for an incompressible, steady-state flow in the non-dimensional form are given as:

$$\begin{cases} \nabla \cdot \left(\boldsymbol{u}\boldsymbol{u}^{\top}\right) = \nabla \cdot \bar{\boldsymbol{\sigma}}\left(\boldsymbol{u}, p\right) + \boldsymbol{f} & \text{in } \Omega \\ \nabla \cdot \boldsymbol{u} = 0 & \text{in } \Omega \\ \boldsymbol{u} = \boldsymbol{u}_{\mathrm{D}} & \text{on } \Gamma_{\mathrm{D}} \\ \bar{\boldsymbol{\sigma}}\left(\boldsymbol{u}, p\right) \cdot \boldsymbol{n} = \boldsymbol{0} & \text{on } \Gamma_{\mathrm{N}}, \end{cases} \tag{1}$$

where $\boldsymbol{n}$ is the unit outward normal vector on the boundary, and $\boldsymbol{u}$, p, $\boldsymbol{f}$, and ∇ denote the non-dimensional velocity, pressure, body force, and gradient operator, respectively. These non-dimensional quantities are defined as follows:

$$\boldsymbol{u} = \frac{\boldsymbol{u}^*}{U},\ p = \frac{p^*}{\rho U^2},\ \boldsymbol{f} = \frac{L}{U^2}\boldsymbol{f}^*,\ \nabla = L\nabla^*, \tag{2}$$

where U and L are the characteristic velocity and length, ρ and ν are the fluid density and dynamic viscosity, and $*$ denotes the dimensional quantities. The fluid stress tensor $\bar{\boldsymbol{\sigma}}\left(\boldsymbol{u}, p\right)$ is defined as follows:

$$\bar{\boldsymbol{\sigma}}\left(\boldsymbol{u}, p\right) := -p\mathbf{I} + \frac{1}{\mathrm{Re}}\left(\nabla\boldsymbol{u} + \nabla\boldsymbol{u}^{\top}\right),\ \mathrm{Re} = \frac{UL}{\nu}. \tag{3}$$

where $\boldsymbol{I}$ is the identity tensor, and Re is the Reynolds number. The boundary $\Gamma := \partial\Omega$ is composed of the Dirichlet boundary Γ_{D}, where a velocity profile is given, and the Neumann boundary Γ_{N}, where the boundary stress vector $\boldsymbol{\sigma} := \bar{\boldsymbol{\sigma}} \cdot \boldsymbol{n}$ is specified as zero.

2.2 Formulation of the density-based topology optimization

In this research, the density-based topology optimization method with filtering and projection is used [Lazarov and Sigmund, 2011, Wang et al., 2011, Kawamoto et al., 2011]. A pseudo-density

field $\gamma(\boldsymbol{x})$, which is a continuous function defined in $[0,1]$, is introduced to describe the material distribution. To perform topology optimization, we consider the computational domain Ω which consists of the solid sub-domain Ω_{s} and the fluid sub-domain Ω_{f}. The solid domain Ω_{s} is defined as the domain where $\gamma = 0$, and the fluid domain Ω_{f} is defined as the domain where $\gamma = 1$.

$$\gamma(\boldsymbol{x}) = \begin{cases} 0 \text{ in } \Omega_{\mathrm{s}} \\ 1 \text{ in } \Omega_{\mathrm{f}}. \end{cases} \tag{4}$$

The density filtering is employed to prevent numerical instabilities in topology optimization. The filtered density field $\tilde{\gamma}$ is obtained as the solution of the following Helmholtz-type partial differential equation.

$$\begin{cases} -r^2\nabla^2\tilde{\gamma} + \tilde{\gamma} = \gamma & \text{in } \Omega \\ \nabla\tilde{\gamma}\cdot\boldsymbol{n} = 0 & \text{on } \Gamma, \end{cases} \tag{5}$$

where r denotes the filter radius. Finally, the projected density field $\hat{\gamma}$ is obtained by applying the smoothed Heaviside function $H(\tilde{\gamma};\eta,\beta)$ as follows:

$$\hat{\gamma} := H(\tilde{\gamma};\eta,\beta) = \frac{\tanh(\beta\eta) + \tanh(\beta(\tilde{\gamma}-\eta))}{\tanh(\beta\eta) + \tanh(\beta(1-\eta))}, \tag{6}$$

where η and β denote the threshold and the sharpness parameters, respectively. Fig. 1 shows a plot of the smoothed Heaviside function for different β.

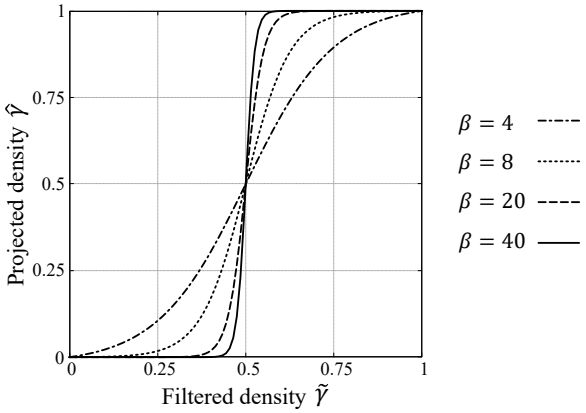

Fig. 1: Smoothed Heaviside function $H(\tilde{\gamma};\eta,\beta)$, $\eta = 0.5$

In order to make the governing equations to be applicable in the entire fixed design domain, a fictitious force $\boldsymbol{f} = -\alpha\boldsymbol{u}$ is introduced based on the Darcy law (also called the Brinkman model) [Borrvall and Petersson, 2003].

$$\begin{cases} \nabla\cdot\left(\boldsymbol{u}\boldsymbol{u}^{\top}\right) = \nabla\cdot\bar{\boldsymbol{\sigma}}(\boldsymbol{u},p) - \alpha(\hat{\gamma})\boldsymbol{u} & \text{in } \Omega \\ \nabla\cdot\boldsymbol{u} = 0 & \text{in } \Omega \\ \boldsymbol{u} = \boldsymbol{u}_{\mathrm{D}} & \text{on } \Gamma_{\mathrm{D}} \\ \bar{\boldsymbol{\sigma}}(\boldsymbol{u},p)\cdot\boldsymbol{n} = \boldsymbol{0} & \text{on } \Gamma_{\mathrm{N}}, \end{cases} \tag{7}$$

The solid domain is represented as a porous material, where the inverse permeability $\alpha(\hat{\gamma})$ takes the value much greater than 1. In this work, the function $\alpha(\hat{\gamma})$ is defined as follows:

$$\alpha(\hat{\gamma}) = \alpha_{\max}(1-\hat{\gamma}), \tag{8}$$

where $\alpha_{\max}$ is the maximum value of the inverse permeability.

2.3 Geometric constraint for excluding "floating" islands

As has been discussed In Section 1, "floating" solid regions entirely surrounded by the fluid may be nucleated in the design problem of fluid diodes. In order to obtain wall-connected structures in the fluid topology optimization, we must eliminate such "floating" solid regions or make them connected to some fixed parts, e.g., no-slip wall boundaries. Therefore, we introduce a geometric constraint for excluding "floating" islands based on the fictitious physical model [Yamada and Noguchi, 2022].

The key point is to set up a boundary value problem similar to a heat conduction problem where the floating solid regions are detected as the hot portion in the solution. The governing equations for the fictitious temperature field T are defined as follows:

$$\begin{cases} \nabla\cdot(d(\hat{\gamma})\nabla T) + (1-\hat{\gamma}-T) = 0 & \text{in } \Omega \\ T = 0 & \text{on } \Gamma_T \\ d\nabla T\cdot\boldsymbol{n} = 0 & \text{on } \Gamma_q, \end{cases} \tag{9}$$

where d is the diffusion coefficient defined as:

$$d(\hat{\gamma}) = d_{\max} + (d_{\min} - d_{\max})\hat{\gamma}. \tag{10}$$

The diffusion coefficient d is is made to take a large value $d_{\max}$ in the solid domain and a small value

$d_{\min}$ in the fluid domain. There is a heat source of $O(1)$ in the solid domain and no heat source in the fluid domain. Also, the fictitious temperature value is set to zero on the Dirichlet boundary Γ_T to which all the solid regions are expected to be connected.

Under this problem setup, in the solid regions connected to a Dirichlet boundary Γ_T, heat is transferred instantaneously by the very high diffusion coefficient $d_{\max}$, and the fictitious temperature becomes nearly zero. But in the solid regions not connected to the Dirichlet boundary Γ_T, heat cannot be transferred anywhere since it is surrounded by the fluid region with very low conductivity $d_{\min}$, and the fictitious temperature takes the value around one. In this way, "floating" islands can be detected as regions with fictitious temperature of $O(1)$.

In addition, to restrict these floating solid regions, the following cost function is introduced:

$$J_{\mathrm{h}} = \int_{\Omega} (1 - \hat{\gamma}) T^2 \mathrm{d}\Omega. \tag{11}$$

It should be noted that, as mentioned in the work of Yamada and Noguchi [2022], the choice of the cost function J_{h} is not unique. This function (11) is expressed as the integral of the square of the temperature in the solid domain Ω_{s} and is expected to have a large value when there is a floating solid region. Then, setting a sufficiently small upper bound for this cost function can constrain the nucleation of those "floating" solid regions.

2.4 Optimum design of fluid diodes with the geometric constraint for excluding "floating" islands

Let $\boldsymbol{u}_{\mathrm{f}}$, p_{f} denote the state variables representing the fluid velocity and pressure in the forward flow, respectively. Similarly, let $\boldsymbol{u}_{\mathrm{r}}$, p_{r} denote those in the reverse flow. The viscous energy dissipation can be evaluated as the boundary integral of total pressure flux as follows:

$$J_{\mathrm{f}} = -\int_{\Gamma} \left(p_{\mathrm{f}} + \frac{\boldsymbol{u}_{\mathrm{f}} \cdot \boldsymbol{u}_{\mathrm{f}}}{2} \right) (\boldsymbol{u}_{\mathrm{f}} \cdot \boldsymbol{n}) \, \mathrm{d}\Gamma, \tag{12}$$

$$J_{\mathrm{r}} = -\int_{\Gamma} \left(p_{\mathrm{r}} + \frac{\boldsymbol{u}_{\mathrm{r}} \cdot \boldsymbol{u}_{\mathrm{r}}}{2} \right) (\boldsymbol{u}_{\mathrm{r}} \cdot \boldsymbol{n}) \, \mathrm{d}\Gamma, \tag{13}$$

where J_{f} and J_{r} denote the energy dissipation of the forward and the reverse flow, respectively. It should be noted that this expression in boundary integral form is identical to that in domain integral form used in the previous works [Lin et al., 2015, Sato et al., 2017a], see Appendix A.

In the most previous works, the diodicity, the ratio of the pressure drop in the reverse flow to that in the forward flow, is used as a performance indicator for fluid diodes.

$$\mathrm{Di} = \frac{\Delta p_{\mathrm{r}}}{\Delta p_{\mathrm{f}}} \tag{14}$$

According to the previous study [Lin et al., 2015], the diodicity can also be defined using the energy dissipation as follows:

$$\mathrm{Di}' = \frac{J_{\mathrm{r}}}{J_{\mathrm{f}}} = \frac{-\int_{\Gamma} \left(p_{\mathrm{r}} + \frac{\boldsymbol{u}_{\mathrm{r}} \cdot \boldsymbol{u}_{\mathrm{r}}}{2} \right) (\boldsymbol{u}_{\mathrm{r}} \cdot \boldsymbol{n}) \, \mathrm{d}\Gamma}{-\int_{\Gamma} \left(p_{\mathrm{f}} + \frac{\boldsymbol{u}_{\mathrm{f}} \cdot \boldsymbol{u}_{\mathrm{f}}}{2} \right) (\boldsymbol{u}_{\mathrm{f}} \cdot \boldsymbol{n}) \, \mathrm{d}\Gamma} \approx \mathrm{Di}. \tag{15}$$

A large value of the diodicity Di' indicates a significant difference between the energy lost in the forward and the reverse flows, quantifying the directionality of the flow.

However, as mentioned in [Sato et al., 2017a], a fluid diode with high diodicity is not always an appropriate design. It is desirable to avoid excessive energy dissipation in the forward flow to mitigate the driving force. From this standpoint, we formulate the optimal design problem of maximizing the energy dissipation in the reverse flow subject to a maximum allowed energy dissipation in the forward flow. Assuming that this constraint becomes active in the process of maximizing the energy dissipation in the reverse flow, this problem is equivalent to the problem for maximizing diodicity. In addition, to restrict the floating solid regions, a geometric constraint is introduced using the fictitious physical model, cf. (9).

Finally, the optimization problem is described as follows:

$$\underset{\gamma}{\text{minimize}} \quad J = -J_{\mathrm{r}} \tag{16}$$

$$\text{subject to:} \quad G_1 = J_{\mathrm{f}} - J_{\mathrm{f,max}} \leq 0 \tag{17}$$

$$G_2 = J_{\mathrm{h}} - J_{\mathrm{h,max}} \leq 0 \tag{18}$$

$$0 \leq \gamma \leq 1$$

Governing equations (7) and (9),

where $J_{\mathrm{f,max}}$ and $J_{\mathrm{h,max}}$ are the upper bound values of J_{f} and J_{h}, respectively. The boundary conditions for the forward flow $\boldsymbol{u}_{\mathrm{f}}$, p_{f}, the reverse flow $\boldsymbol{u}_{\mathrm{r}}$, p_{r}, and the fictitious temperature field T are described as follows:

$$\begin{cases} \boldsymbol{u}_{\mathrm{f}} = \boldsymbol{u}_{\mathrm{in,f}} & \text{on } \Gamma_{\mathrm{in,f}} \\ \boldsymbol{u}_{\mathrm{f}} = \boldsymbol{0} & \text{on } \Gamma_{\mathrm{wall}} \\ \bar{\boldsymbol{\sigma}}\left(\boldsymbol{u}_{\mathrm{f}}, p_{\mathrm{f}}\right) \cdot \boldsymbol{n} = \boldsymbol{0} & \text{on } \Gamma_{\mathrm{out,f}} \\ \boldsymbol{u}_{\mathrm{r}} = \boldsymbol{u}_{\mathrm{in,r}} & \text{on } \Gamma_{\mathrm{in,r}} \\ \boldsymbol{u}_{\mathrm{r}} = \boldsymbol{0} & \text{on } \Gamma_{\mathrm{wall}} \\ \bar{\boldsymbol{\sigma}}\left(\boldsymbol{u}_{\mathrm{r}}, p_{\mathrm{r}}\right) \cdot \boldsymbol{n} = \boldsymbol{0} & \text{on } \Gamma_{\mathrm{out,r}} \\ T = 0 & \text{on } \Gamma_T \\ d\nabla T \cdot \boldsymbol{n} = 0 & \text{on } \Gamma_q, \end{cases} \tag{19}$$

where $\Gamma_{\mathrm{in,f}}$ and $\Gamma_{\mathrm{out,f}}$ represent the inlet and the outlet for the forward flow, and $\Gamma_{\mathrm{in,r}}$ and $\Gamma_{\mathrm{out,r}}$ represent those for the reverse flow, respectively. The inlet of the forward flow $\Gamma_{\mathrm{in,f}}$ corresponds to the outlet of the reverse flow $\Gamma_{\mathrm{out,r}}$, and the outlet of the forward flow $\Gamma_{\mathrm{out,f}}$ corresponds to the inlet of the reverse flow $\Gamma_{\mathrm{in,r}}$. For the fictitious physical field, the Dirichlet boundary Γ_T corresponds to the portion of the wall boundary Γ_{wall} that is adjacent to the design domain, while the other boundaries $\Gamma \setminus \Gamma_T$ are considered as the Neumann boundary Γ_q.

The sensitivities of J, G_1 and G_2 with respect to the design variable γ are derived based on the continuous adjoint approach. Adjoint equations should be solved in each optimization step, and the sensitivities are calculated using both state and adjoint variables. See Appendix B for details on the adjoint systems and the sensitivities.

3 Implementation details

3.1 Implementation in OpenFOAM

As mentioned above, topology optimization of fluid diode design requires forward and reverse flow simulations and the solutions of their adjoint equations. Furthermore, the computational costs of three-dimensional fluid analysis are considerably higher than that of two-dimensional analysis. To mitigate such computational burdens, efficient fluid analysis methods must be employed.

In this work, we employed an open-source finite volume software, OpenFOAM v5, to discretize the PDEs. A Semi-Implicit Method for Pressure Linked Equation (SIMPLE) algorithm was used to solve Navier-Stokes equations. Adjoint Navier-Stokes equations were also solved using a SIMPLE-type algorithm based on the work done by Othmer [2008]. The fictitious heat equation was solved based on the implementation of laplacianFoam, a default solver for heat equations in OpenFOAM.

3.2 Optimization algorithm

The optimization procedure is described in Algorithm 1. First, we prepare a mesh for computational domain and optimization parameters, such as upper bound values of the constraint functions. Then, we decompose the computational domain for parallel computing, declare unknowns, initialize the psuedo density field γ, and compute $\tilde{\gamma}$ from (5), and $\hat{\gamma}$ from (6). Material properties such as the inverse permeability α and the fictitious thermal conductivity d are interpolated using the projected density field $\hat{\gamma}$ from (8) and (10).

Next, the optimization loop starts by solving governing equations of primal problems, i.e., Navier-Stokes equations for forward and reverse flows (7) and the fictitious heat equation (9). Then, objective function (16) and constraint functions (17) and (18) are evaluated. If the convergence criterion is satisfied, the optimization is terminated. Otherwise, the adjoint governing equations of forward and reverse flows and fictitious heat problems are solved. Sensitivities with respect to the projected density $\hat{\gamma}$ are computed using primal and adjoint variables. We apply the chain rule to obtain the sensitivities with respect to the density γ. The density field γ is updated using the Method of Moving Asymptotes (MMA) [Svanberg, 1987]. Then, the filtered density $\tilde{\gamma}$ and the projected density $\hat{\gamma}$ are obtained from the filtering (5) and projection (6). Material properties α and d are interpolated using the updated projected density $\hat{\gamma}$ from (8) and (10).

In this work, the following continuation method is employed for sharpness parameter β of Heaviside function (6).

$$\beta_t = \begin{cases} 8.0 & (1 \leq t < 100) \\ \min(40,\ \beta_{t-1} + 0.1) & (t \geq 100), \end{cases} \tag{20}$$

where the subscript t denotes the iteration number. Also, the threshold parameter η of Heaviside function (6) is chosen as 0.5.

The above procedure is repeated until the following criterion is satisfied: after the continuation method is finished, the relative difference between the objective function value of current and previous time steps becomes smaller than ε_c while the constraints are satisfied.

Numerical computations in this paper are performed on a Linux computer with 20 Intel Xeon Gold 6242R CPU cores (3.10GHz).

4 Numerical examples

4.1 Validation of the fictitious physical model

In this section, we performed two-dimensional numerical analysis on the proposed fictitious physical model. The target geometry is shown in Fig. 2, whose boundary is set as Dirichlet boundary Γ_T where $T = 0$. The size of the domain is set as 1.5×2.0.

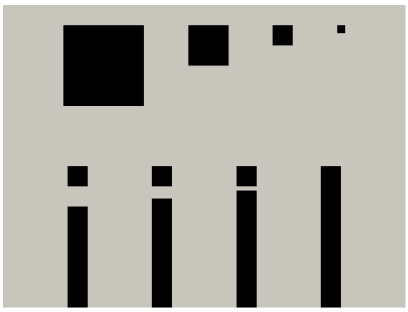

Fig. 2: Target geometry for validation of the fictitious physical field. Black region represents solid $\gamma = 0$ and white region represents fluid $\gamma = 1$. Every boundary is considered as $\Gamma = \Gamma_T$ where $T = 0$.

Fig. 3 shows fictitious temperature fields for different sets of maximum and minimum diffusion coefficients, and Fig. 4 shows the corresponding sensitivity distributions of J_h. The aim of the fictitious physical model is to detect the "floating" islands as regions with high value of T. The solid domain connected to the outer boundaries and the fluid domain should have a value of T close to 0, so that only the structures without wall connectivity will be penalized by the geometric constraint. Taking this into account, the maximum value of diffusion coefficient d_max should be sufficiently large and the minimum value of diffusion coefficient d_min should be sufficiently small.

However, in the case with $d_\mathrm{max} = 1 \times 10^3$ such as Figs. 3o and t, the value of T in the "floating" islands becomes smaller compared to the result with $d_\mathrm{max} = 1 \times 10^2$, because of the excessively large maximum value of diffusion coefficient. Another characteristic of the fictitious physical field is its dependence on the size of the floating solid regions. In the fictitious physical model proposed in [Yamada and Noguchi, 2022], it was reported that the void region takes $T = 1$ regardless of its size. Although this feature is desirable in detection, our formulation may have an advantage in the context of capturing the boundaries of "floating" islands, which is discussed in Appendix C. From the above observations, it can be concluded that the proposed fictitious physical model is effective in detecting "floating" islands, and that the maximum value of diffusion coefficient should be $1 \times 10^1 \leq d_\mathrm{max} \leq 1 \times 10^2$ and the minimum value of diffusion coefficient should be $d_\mathrm{min} \leq 1 \times 10^{-5}$.

Next, to verify the effectiveness of the cost function (11), we performed a non-constrained optimization problem of minimizing J_h. For this numerical example, the steepest decent method with a constant step size was employed as the optimizer, and the sensitivity of J_h was normalized by its absolute maximum value at each time step. Here, we chose the diffusion coefficients as $(d_\mathrm{max}, d_\mathrm{min}) = (1 \times 10^1, 1 \times 10^{-5})$. Figs. 5 and 6 show the history of density distribution and the history of evaluation function J_h, respectively. In the first 20 iterations, most solid regions either vanished or were connected to the outer boundary Γ_T, then the solid regions gradually decreased, and after approximately 80 iterations, the solid regions vanished completely. The cost function J_h also decreased monotonically during the optimization. Consequently, we confirm that the proposed fictitious physical model and the cost function J_h can penalize the "floating" islands. It is worth noting that those d_min and d_max should be chosen carefully depending on the the problem-at-hand, because they affect how the floating structures will be modified by the geometric constraint, i.e.,

Algorithm 1: Optimization problem of fluid diodes with the geometric constraint for excluding "floating" islands

input: mesh, optimization parameters

initialization:
decompose the computational domain for parallel computing
declare unknowns
initialize the density fields γ, $\tilde{\gamma}$, and $\hat{\gamma}$
interpolate material properties α and d
begin
  for $it = 0; it < Maxloop; it = it + 1$ **do**
    solve Navier–Stokes equations for forward flow using the SIMPLE algorithm
    solve Navier–Stokes equations for reverse flow using the SIMPLE algorithm
    solve fictitious heat conduction equation
    evaluate objective and constraint functions
    if $\left\| \frac{J_{it} - J_{it-1}}{J_{it}} \right\| < \varepsilon_c, G_1 < 0, G_2 < 0$ **then**
      break;
    else
      solve adjoint Navier–Stokes equations for forward flow using the SIMPLE algorithm
      solve adjoint Navier–Stokes equations for reverse flow using the SIMPLE algorithm
      solve adjoint fictitious heat conduction equation
      calculate sensitivities
      update the density field γ using MMA
      solve PDE-filter to get $\tilde{\gamma}$
      adopt Heaviside projection to get $\hat{\gamma}$
      interpolate material properties α and d
    end
  end
end

whether the "floating" islands will disappear or be connected to the outer boundaries.

4.2 Three-dimensional design of fluid diodes with symmetric condition

In this section, optimizations of fluid diodes with and without the geometric constraint (18) were performed. Fig. 7a shows the overall view of the channel to be considered in this numerical example. Fig. 7b shows the computational domain and the boundary conditions for the fluid problem. To avoid excessive computational costs, we handle a quarter model of the entire domain and assume symmetry of the structure in this case. The computational domain was discretized with $906,250$ structured hexahedral cells. For parallel computing, the computational domain was decomposed into 12 subdomains. In this work, the characteristic length L and the characteristic velocity U represent the inlet width and the average velocity at the inlet, respectively, and an incompressible flow with Reynolds number Re of 100 is assumed. Before optimization, the energy dissipation of the channel was evaluated and found to be approximately 0.25 assuming pure fluid phase in the computational domain. Based on the simulation result, the upper bound value of the energy dissipation in the forward flow $J_{\mathrm{f,max}}$ was set to 1.0. The maximum value of inverse permeability $\alpha_{\max}$ was set to 1.0×10^3. For parameters of density filtering, the filter radius r was set to 1.7×10^{-2}, which corresponds to the length of 3 cells. For convergence criteria, $\varepsilon_c = 1 \times 10^{-5}$ was used. The initial guess was given as an uniform distribution $\gamma = 0.5$ in the design domain.

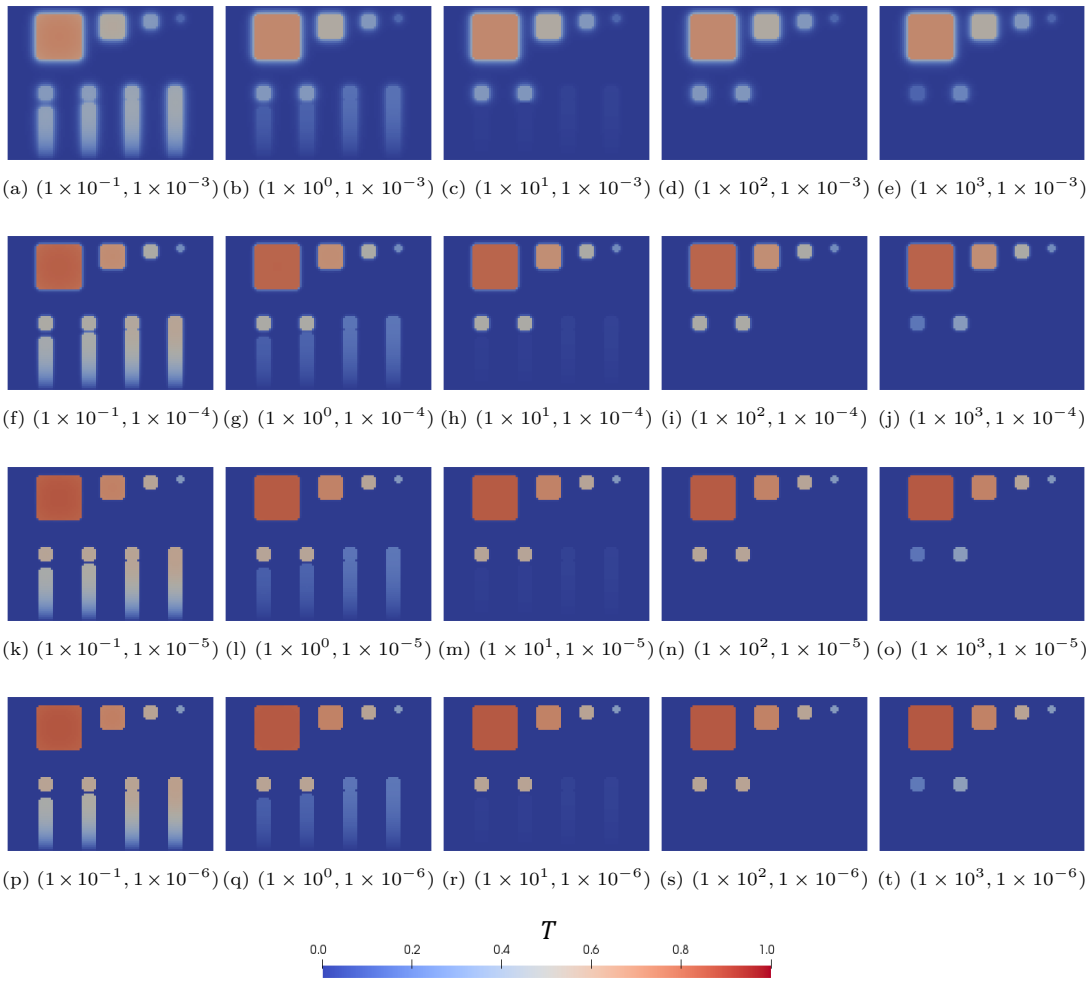

Fig. 3: Fictitious physical field T for various diffusion coefficients $(d_{\max}, d_{\min})$

Boundary conditions for the fictitious physical field are shown in Fig. 8, where the wall adjacent to the design domain is considered as the Dirichlet boundary Γ_T. The parameters for the fictitious physical field were set as $d_{\max} = 1 \times 10^2$ and $d_{\min} = 1\times10^{-5}$ based on the result of the previous Section 4.1. Although the geometric constraint (18) was not imposed in Section 4.2.1, the function value (11) was evaluated for the comparative studies in later sections.

4.2.1 Optimization results without the geometric constraint

Fig. 9 shows the obtained configuration of a fluid diode plotted by the isovolume of $\hat{\gamma} \in [0, 0.5]$, where Figs. 9a and b show the quarter and half model of the entire design, and Figs. 9c and d show streamlines of the forward and reverse flows, all respectively. Fig. 10 shows the optimization history of J_{f}, J_{r}, and J_{h}. The convergence criteria was satisfied in 458 optimization iterations. From Figs. 9c and d, it can be seen that the flow has generally straight paths from the inlet to the outlet in the forward flow, while the flow is bent by inertial forces and the structure, containing many vortices. The solid domains have holes, and exhibit a wall-like structure that separates the design domain into the main channel and the outside. These holes and outer spaces seem to be effectively utilized for changing the flow directions

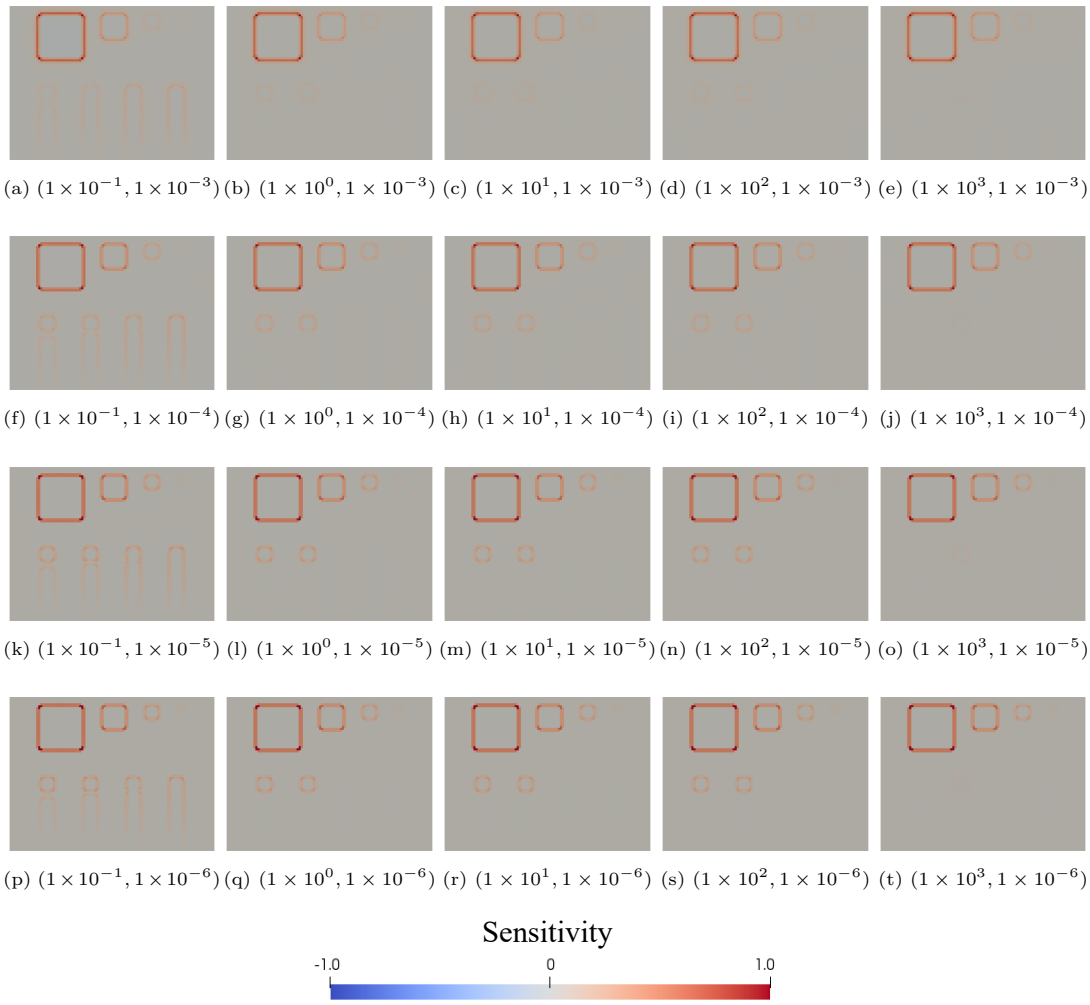

Fig. 4: Sensitivity distributions of the geometric constraint J_{h} for various diffusion coefficients $(d_{\max}, d_{\min})$

in the reverse flow, maximizing the energy dissipation. The energy dissipation in the reverse flow J_{r} increased during the optimization and reached approximately 1.52 at the end of the optimization process. Since the upper bound constraint for the energy dissipation of forward flow $J_{\mathrm{f}} \leq 1.0$ was satisfied with $J_{\mathrm{f}} \approx 1.0$, the diodicity of the obtained structure was Di ≈ 1.52.

Although the optimized result shows a satisfactory diodicity, the structure features floating solid islands, namely, the solid domains without wall connectivity. To manufacture the obtained structure, the design must be modified so that every solid domain can be supported by outer boundaries. One possibility is to remove all "floating" islands, but it is clear that the "floating" regions act an essential role in the enhancement of diodicity in this example. However, it is also challenging for designers to modify it to a freestanding structure while maintaining diodicity, e.g., by adding supports. Therefore, we need to employ a geometric constraint to ensure wall-connected structures for the three-dimensional design of fluid diodes.

The history of function J_{h} is plotted in Fig. 10, and the fictitious physical field over solid regions of the obtained structure is depicted in Fig. 11. It is seen that "floating" islands are detected as

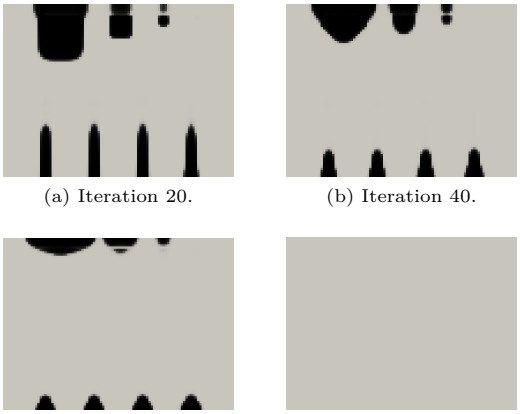

(a) Iteration 20. (b) Iteration 40. (c) Iteration 60 (d) Iteration 80

Fig. 5: Density distribution during minimizing J_h with $(d_\mathrm{max}, d_\mathrm{min}) = (1 \times 10^{1}, 1 \times 10^{-5})$

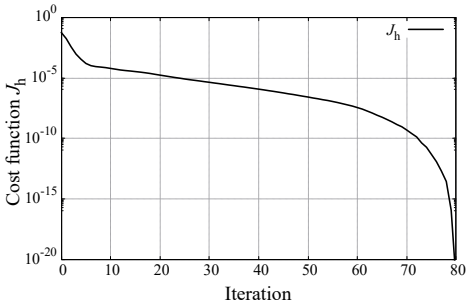

Fig. 6: Optimization history of minimizing J_h

regions with high value of fictitious physical field T. The value of J_h for the final configuration was $J_\mathrm{h} \approx 3.9 \times 10^{-2}$. We call this value as $J_\mathrm{h,ref}$, and we impose a sufficiently smaller upper bound value $J_\mathrm{h,max}$ than $J_\mathrm{h,ref}$ to constrain "floating" islands in the following section.

4.2.2 Optimization results with the geometric constraint

The problem settings and parameters were the same as in Section 4.2.1 except for introducing the geometric constraint (18) into the optimization problem. For the upper bound value $J_\mathrm{h,max}$, 1×10^{-5} was used.

Fig. 12 shows the obtained configuration of a fluid diode with the geometric constraint plotted by the isovolume of $\hat{\gamma} \in [0, 0.5]$, where Figs. 12a and b show the quarter and half model of the

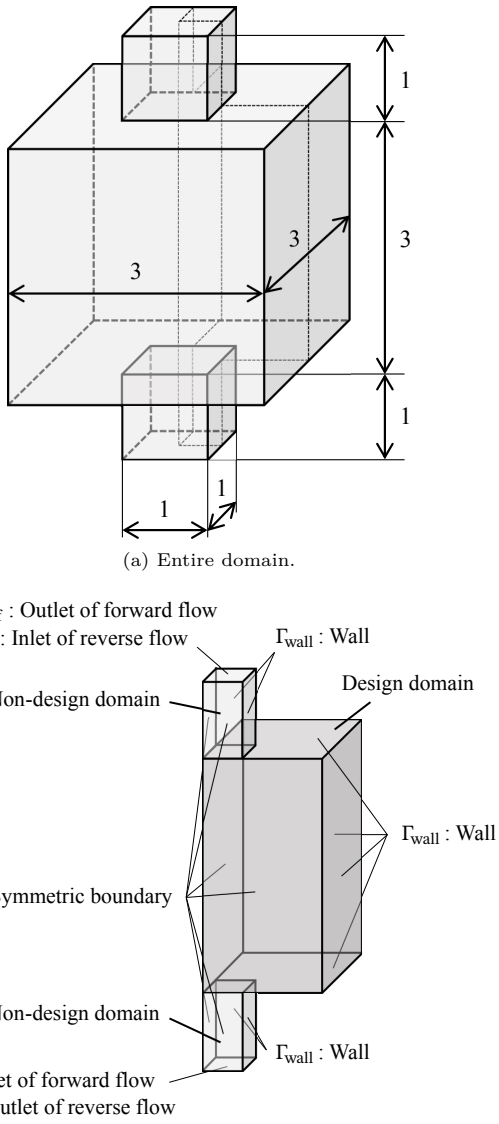

(a) Entire domain.

(b) Quarter model for computation.

Fig. 7: Computational domain and boundary conditions for the fluid flow

entire design, and Figs. 12c and d show streamlines of the forward and reverse flows, respectively. Fig. 13 shows the optimization history of J_f, J_r, and J_h. In this case, the convergence criteria was satisfied in 420 optimization iterations. From Figs. 12c and d, the flow in the obtained structure has features similar to the solution in the previous example, i.e., the fluid flows straight in the forward direction, while the many vortices exist in the reverse flow. Although the number of

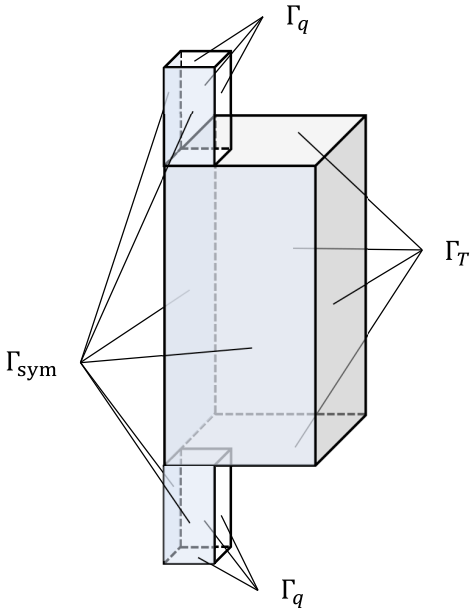

Fig. 8: Boundary conditions for the fictitious physical field

holes appears to be less than that of the structure in Fig. 9, the resulting structure still has a unique topology. The energy dissipation in the reverse flow J_{r} reached approximately 1.63, and the diodicity was Di ≈ 1.63.

The difference between the obtained structures of Figs. 9 and 12 is the existence of floating solid regions. In the solution of Fig. 12, every solid part connects to the outer boundaries, and therefore the structure has wall connectivity. As shown in Fig. 13, the geometric constraint (18) was satisfied while the optimization process of fluid diodes proceeded in the same manner as the case without the geometric constraint. It can be seen that the floating solid regions in Fig. 9 disappeared in this solution since such structure is penalized by the geometric constraint, and instead a structure connecting to the outer boundaries emerged near the inlet of the reverse flow, which significantly changes the direction of the reverse flow. The value of the evaluation function J_{h} of the obtained structure was $J_{\mathrm{h}} \approx 9.1 \times 10^{-6}$. Fig. 14 shows the fictitious temperature field over solid regions. The fictitious temperature field of this result has a quite smaller value than that of the case without the constraint for excluding "floating" islands.

While the geometric constraint worked well in this example, we remark that it is non-trivial to know how to set the upper bound value of the geometric constraint. If the upper bound value is not sufficiently small, the "floating" islands might not be penalized and remain in a solution. However, an overly strict geometric constraint value can lead to numerical instability or significantly affect the original optimization problem. Also, the result considering wall-connected structures has better performance in terms of diodicity, but this is not always the case. Both obtained structures in Figs. 9 and 12 are local optima of the problem, and in the latter case, the geometric constraint may have caused the structure to converge to another local optimum. It can also be observed that the solution contains elongated structures of several cell sizes. This structure might be attributed to the effect of the geometric constraint rather than maximizing diodicity. To prevent such small structures, one can employ the minimum length control technique. We hope to extend our proposed method to a robust methodology that can create three-dimensional manufacturable fluid diodes with high diodicity.

4.3 Full-scale three-dimensional design of fluid diodes

In this section, we present optimization results of full-scale three-dimensional design of fluid diodes with and without the geometric constraint. Fig. 15a shows the overall view of the channel to be considered in this numerical example. Fig. 15b shows the computational domain and the boundary conditions for the fluid problem. As can be seen, the target channel has a three-dimensional torsional structure, and unlike the previous section, symmetry boundary conditions cannot be used. The computational domain was discretized with $3.63 \cdot 10^5$ structured hexahedral cells. For parallel computing, the computational domain was decomposed into 20 subdomains. As in the previous section, a flow with Re $= 100$ is considered. Before optimization, the energy dissipation of the channel was evaluated and found to be approximately 2.08, assuming that the computational domain is composed of pure fluid phase. For this case, the upper bound value of the energy dissipation in the forward flow $J_{\mathrm{f,max}}$ was set to 10. The maximum value of inverse permeability α_{max} was set to 1.0×10^3. For parameters of density filtering, the filter radius r was set to 1.7×10^{-2}.

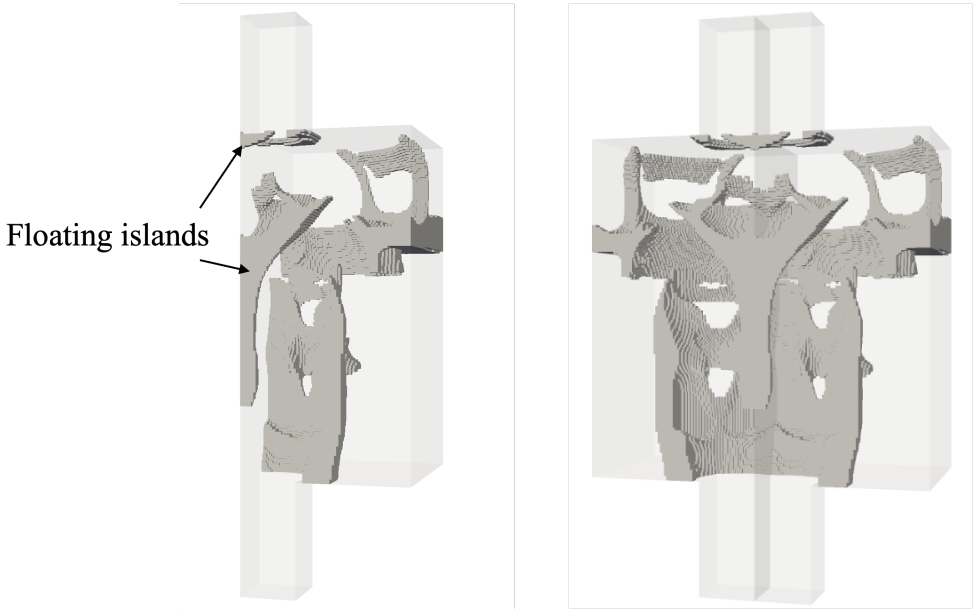

(a) Quarter model. (b) Half model.

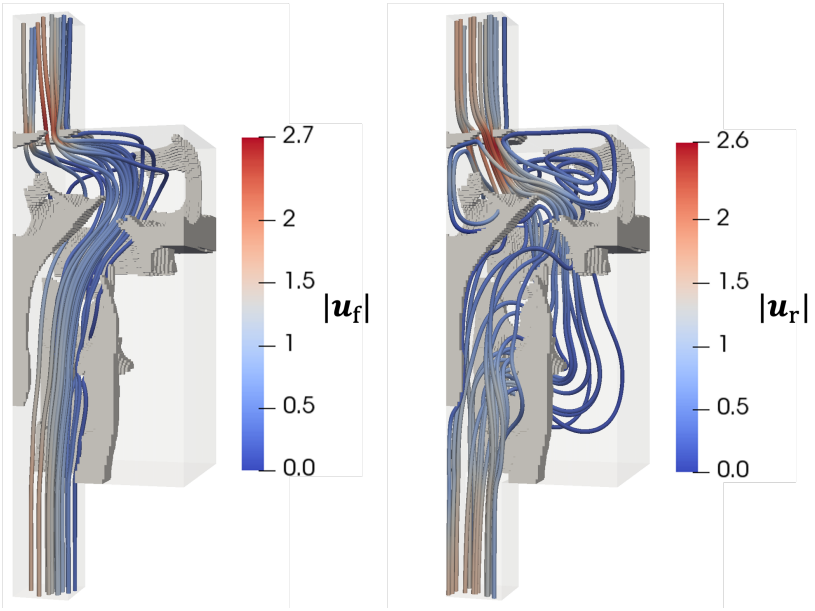

(c) Streamlines of forward flow. (d) Streamlines of reverse flow.

Fig. 9: Obtained configuration without the geometric constraint

The initial guess was uniformly given as $\gamma = 0.5$ in the design domain.

Boundary conditions for the fictitious physical field are shown in Fig. 16. The parameters for the fictitious physical field were set as $d_{\max} = 1 \times 10^2$ and $d_{\min} = 1 \times 10^{-5}$.

4.3.1 Optimization results without the geometric constraint

Fig. 17 shows the obtained configuration of a fluid diode represented by the isovolume of $\hat{\gamma} \in [0, 0.5]$, where Figs. 17a and b show the front and side view

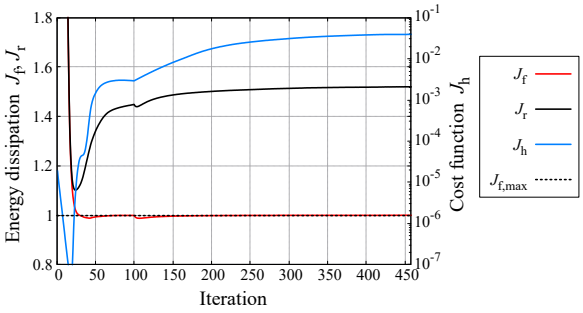

Fig. 10: Optimization history of the result without the geometric constraint

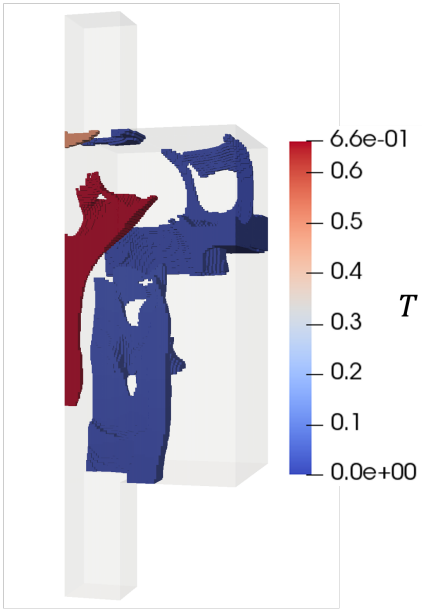

Fig. 11: Fictitious physical field of obtained solution without the geometric constraint. The floating solid domains have high value of the fictitious temperature

of obtained structure, and Figs. 17c and d show streamlines of the forward and reverse flows, all respectively. Fig. 18 shows the optimization history of J_f, J_r, and J_h. The convergence criteria was satisfied in 432 optimization iterations. As in the previous example, it can be seen that the reverse flow contains a relatively large number of vortices. In this example, the obtained structure had the diodicity with Di ≈ 3.53.

However, the obtained result has "floating" islands similar to what has been observed in the previous example in Section 4.2.1. Fig. 19 shows the fictitious physical field on the solid domains. The "floating" solids are detected with large value of T. The history of function J_h is plotted in Fig. 18, and the value of J_h for the final configuration was $J_h \approx 8.8 \times 10^{-3}$.

4.3.2 Optimization results with the geometric constraint

In order to obtain a solution without "floating" islands, we introduced the geometric constraint into this example. In this case, the geometric constraint was used as a post-processing step. That is, using the solution obtained without the geometric constraint in Section 4.3.1 as the initial structure, the optimization problem was solved by adding the geometric constraint. For the upper bound value $J_{h,max}$, 1×10^{-5} was used. For convergence criteria, $\varepsilon_c = 1 \times 10^{-4}$ was used. The sharpness parameter β was set to a constant value of 40.

In this example, it seems to be rather difficult to obtain the solution which fully satisfies the convergence criteria. Given that the objective value was somewhat stabilized after approximately 200 iterations with a slight fluctuation, we therefore terminated the optimization procedure at the 300th iteration. The final structure is shown in Fig. 20 represented by the isovolume of $\hat{\gamma} \in [0, 0.5]$, and the optimization history is plotted in Fig. 21. It shows that the obtained structure contained a relatively large amount of regions with greyscale density. Therefore, the performance of the solution was evaluated by binarizing the density with a threshold value of 0.5. The energy dissipation in the forward flow was $J_f \approx 9.9$, the energy dissipation in the reverse flow was $J_r \approx 34.3$, and the evaluation function of the fictitious field was $J_h \approx 2.9 \times 10^{-5}$. Although the constraint for the fictitious physical field G_2 was violated after binarization, the energy dissipation in the forward flow remained within the constraint. The value of diodicity was Di ≈ 3.47, a slight decrease from the initial structure, cf. Fig. 17.

Fig. 22 shows the fictitious temperature field over solid regions. Compared with the structure in Fig. 19, most of the "floating" islands were successfully eliminated. Nevertheless, there still remain several tiny solid domains without wall connectivity. This can be attributed to the nature of the constraint function Eq. (18). The geometric constraint limits the mean square of the

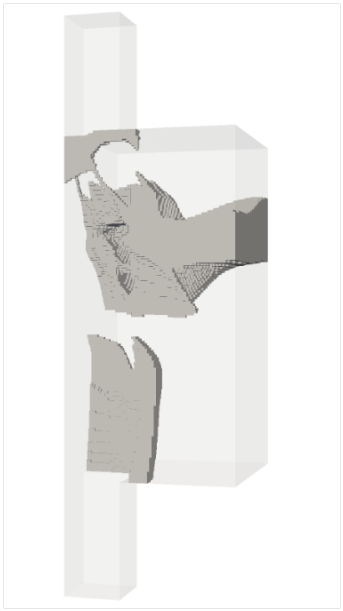

(a) Quarter model.

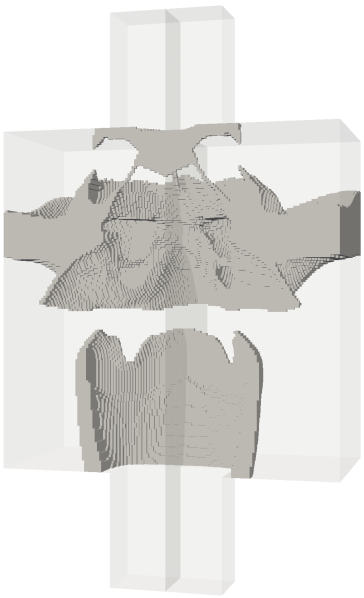

(b) Half model.

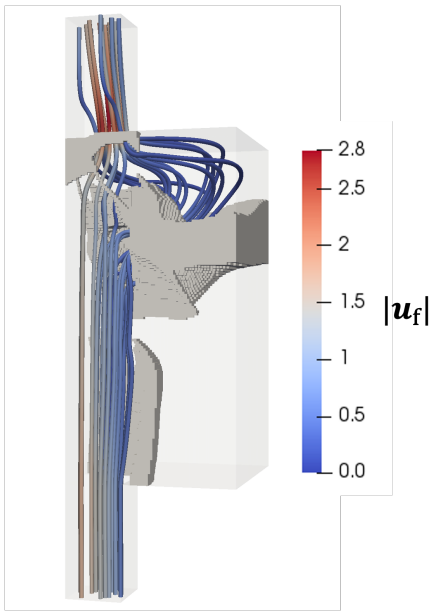

(c) Streamlines of forward flow.

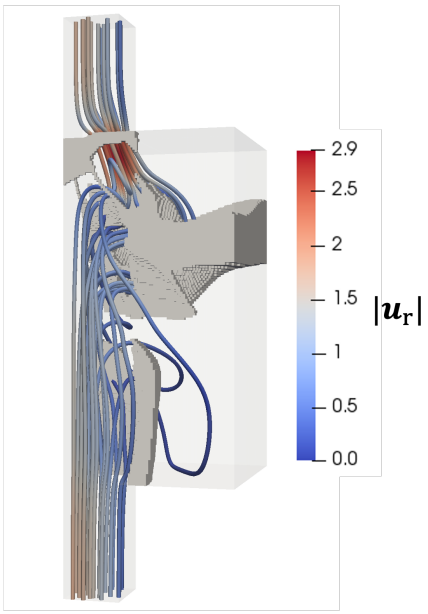

(d) Streamlines of reverse flow.

Fig. 12: Obtained configuration with the geometric constraint $J_{\mathrm{h,max}} = 1 \times 10^{-5}$

fictitious temperature over the solid domain. On the other hand, although small "floating" islands have high fictitious temperatures, their contribution to the mean square temperature is rather insignificant due to their small volumes. As an alternative, an upper constraint on the maximum temperature could be considered, which might effectively exclude "floating" islands by setting an appropriate upper bound temperature.

Furthermore, mesh-size structures are observed in Fig. 19, and this may also be due to the geometric constraint. To mitigate the

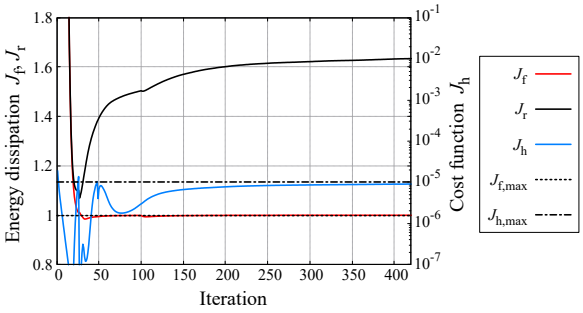

Fig. 13: Optimization history of the result with the geometric constraint $J_{\mathrm{h,max}} = 1 \times 10^{-5}$

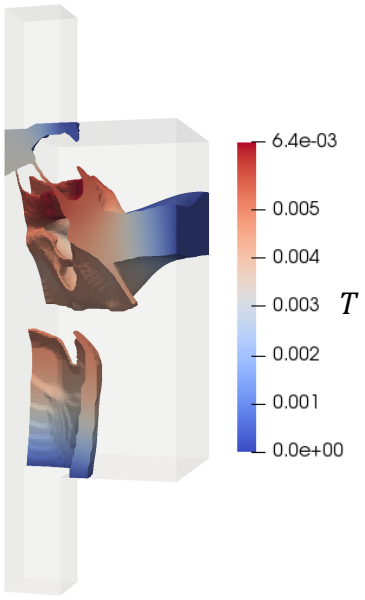

Fig. 14: Fictitious physical field of obtained solution with the geometric constraint $J_{\mathrm{h,max}} = 1 \times 10^{-5}$

mesh size structures, an additional constraint or further regularization would be necessary. As mentioned in Section 4.2.2, the minimum length control technique will work effectively. Employing a larger filter radius or introducing a volume constraint could also be successful. A volume constraint can usually regulate the optimization problem, making it easier to obtain a fluid diode without "floating" islands.

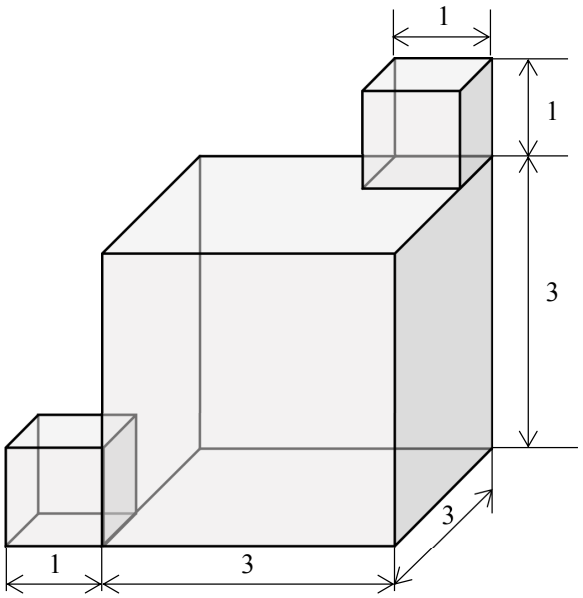

(a) Entire domain

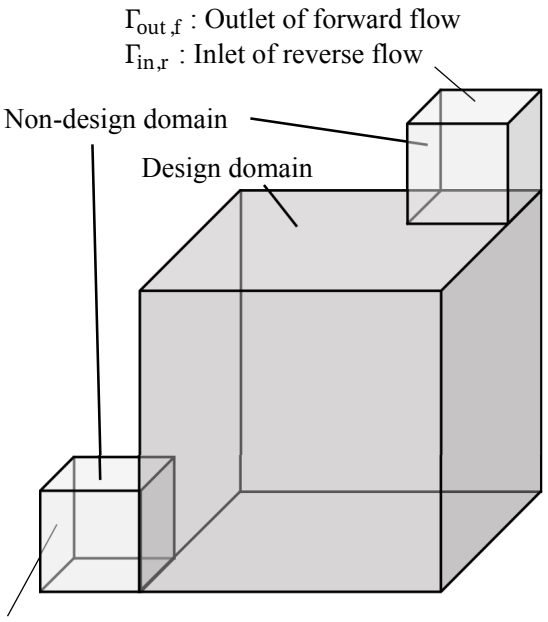

(b) Design domain and boundary conditions for fluid flow

Fig. 15: Computational domain and boundary conditions for the fluid flow of full-scale three-dimensional case

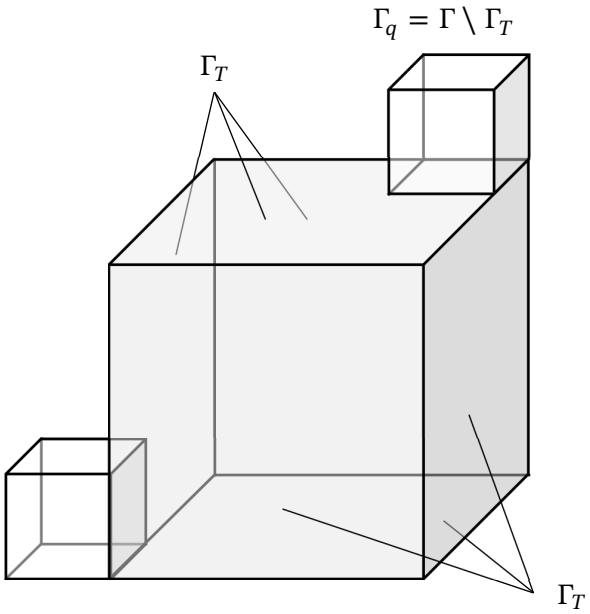

Fig. 16: Boundary conditions for the fictitious physical field

5 Conclusions

In this paper, we proposed a density-based topology optimization method for the three-dimensional design of fluid diodes considering wall-connected structures based on the fictitious physical model approach. One possible problem of three-dimensional design of fluid diodes was the emergence of the "floating" solid domains, the structures without wall connectivity. To deal with this issue, we formulated a fictitious physical model and a geometric constraint to detect and restrict the "floating" solid domains. The main findings are summarized as follows:

1. The optimum design problem of fluid diodes was formulated as maximizing the energy dissipation in the reverse flow subject to the upper bound constraint of the energy dissipation in the forward flow. To detect "floating" islands, the fictitious physical problem was introduced so that the solution has value of $O(1)$ in the "floating" islands and a near-zero value in the other regions. To restrict the "floating" islands, the upper bound constraint was introduced for the integral of the square of the fictitious temperature in the solid domains. The sensitivities were derived based on continuous adjoint method and computed by solving primal and adjoint equations. All the numerical simulations were implemented using OpenFOAM.
2. The proposed fictitious physical model was investigated through the two-dimensional example. As a result, our model has proved to be able to detect the "floating" solids by adjusting the maximum and the minimum value of the diffusion coefficient to an appropriate value. Unlike the fictitious model in previous work, the fictitious temperature has a larger value in large solid domains than in smaller ones. Also, our proposed constraint function for excluding floating solids could successfully eliminate them during the optimization.
3. We first performed topology optimization for designing three-dimensional fluid diodes without the geometric constraints in the two types of channels. In both cases, the obtained structures showed diodicity of Di $>$ 1 within the constraint for the energy dissipation of forward flow. Nevertheless, our numerical examples demonstrated that the solutions of three-dimensional fluid diodes can contain "floating" solid islands and therefore they cannot be manufactured. Meanwhile, those "floating" islands were detected clearly through the proposed fictitious physical model.
4. We then applied our formulation to design fluid diodes considering wall-connected structures. In the symmetric test case, the optimization procedure was initialized by a uniform density distribution, and in the non-symmetric test case, we performed optimization from the obtained result without the geometric constraint. As a result, our method obtained the solutions without "floating" islands while the relatively high diodicity was maintained. Although we observed that mesh-size structures emerged as a side effect of the geometric constraint, the solutions had similar performance to those without wall connectivity and had no or much smaller "floating" islands.

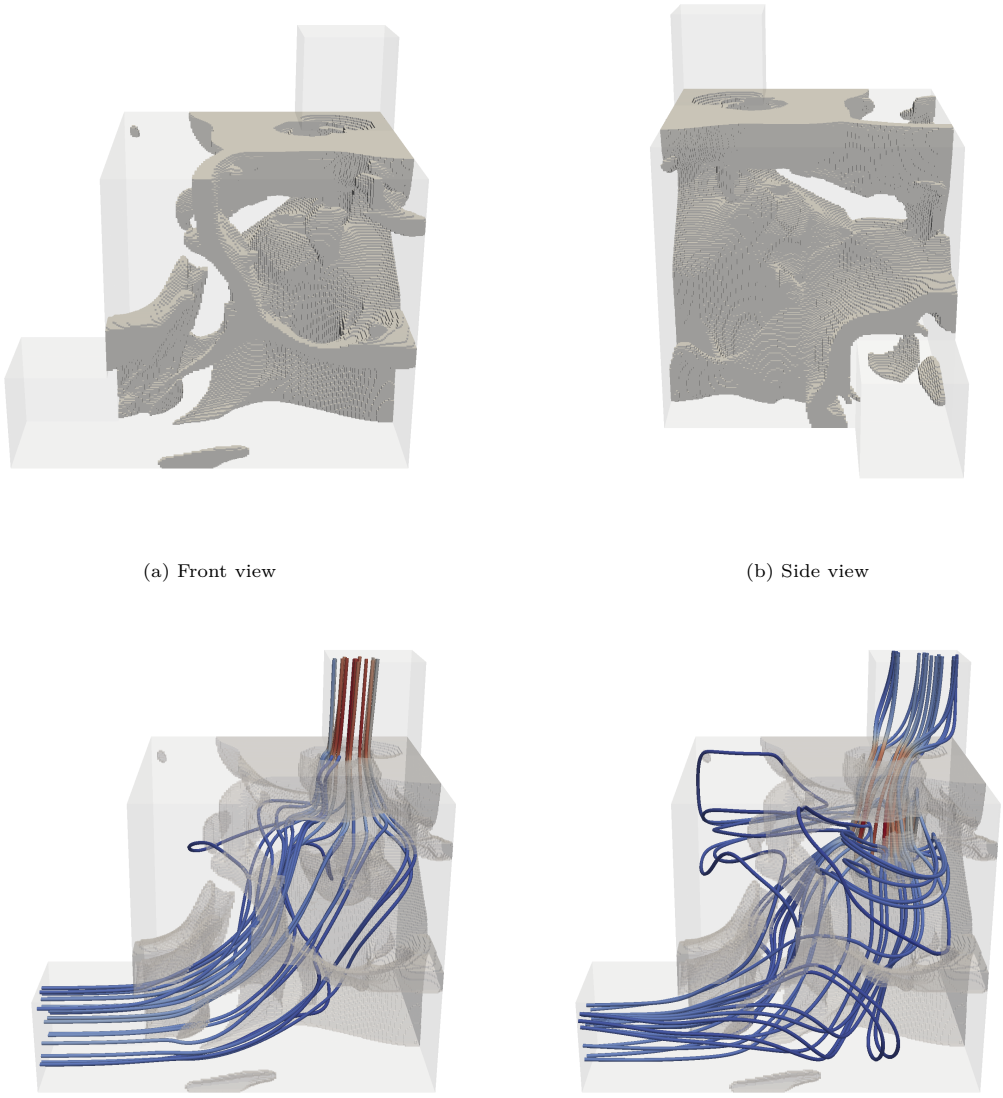

(a) Front view

(b) Side view

(c) Streamlines of forward flow

(d) Streamlines of reverse flow

Fig. 17: Obtained configuration without the geometric constraint in full-scale 3D case

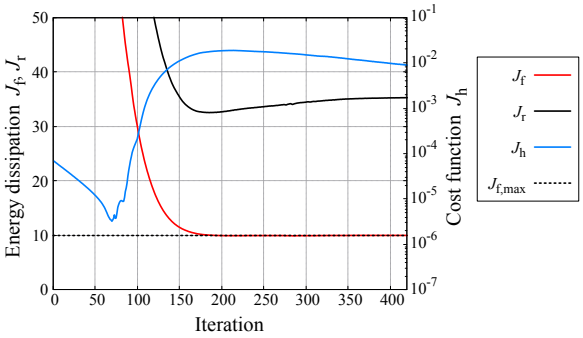

Fig. 18: Optimization history of the result without the geometric constraint in full-scale 3D case

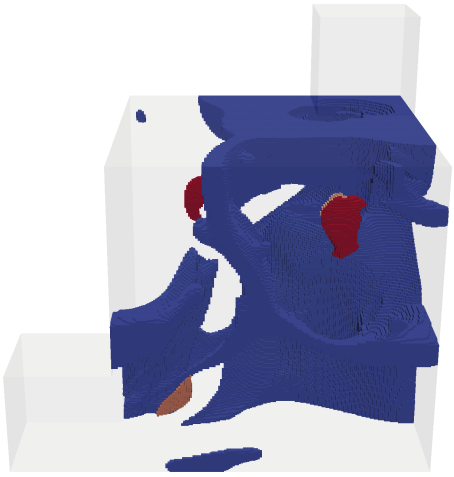

Fig. 19: Fictitious physical field of obtained solution without the geometric constraint

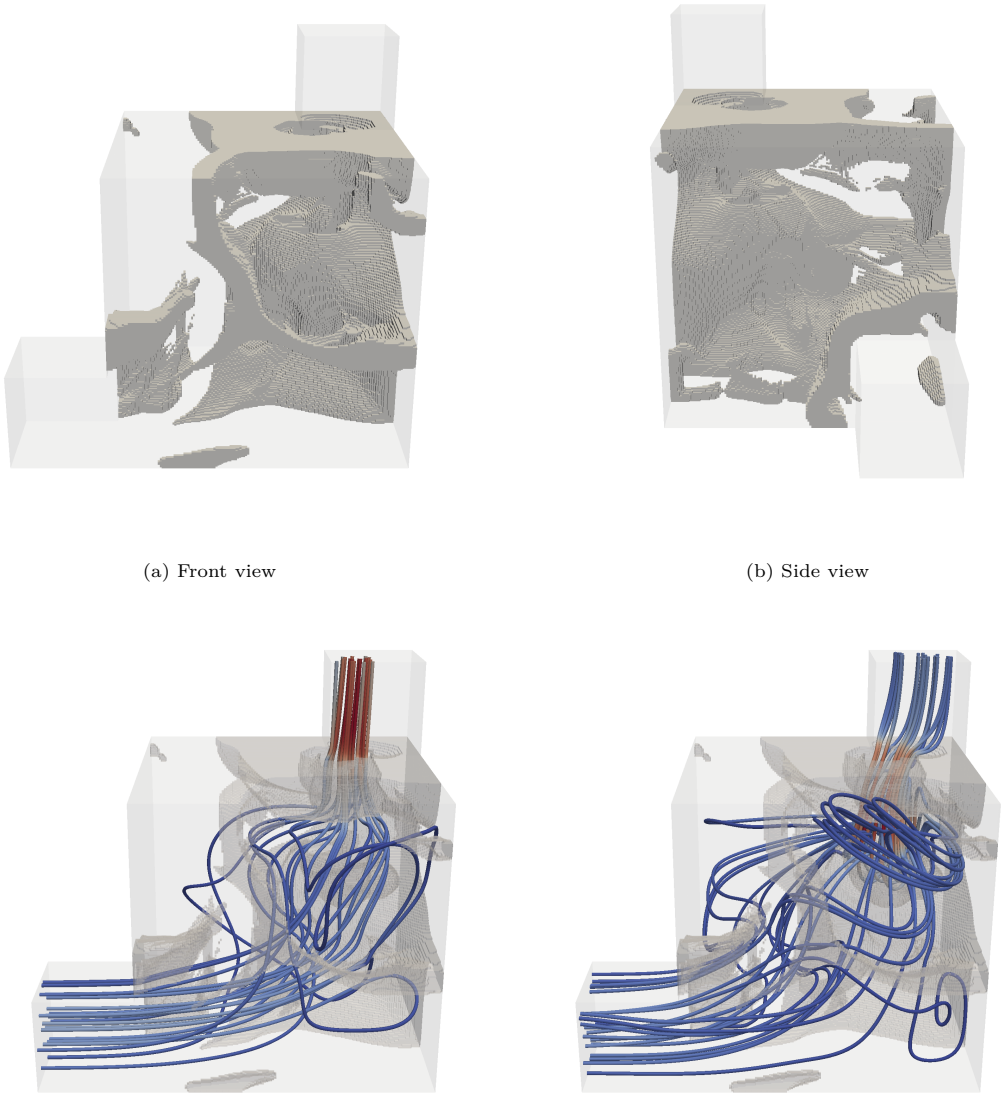

(a) Front view

(b) Side view

(c) Streamlines of forward flow

(d) Streamlines of reverse flow

Fig. 20: Obtained configuration with the geometric constraint in full-scale 3D case

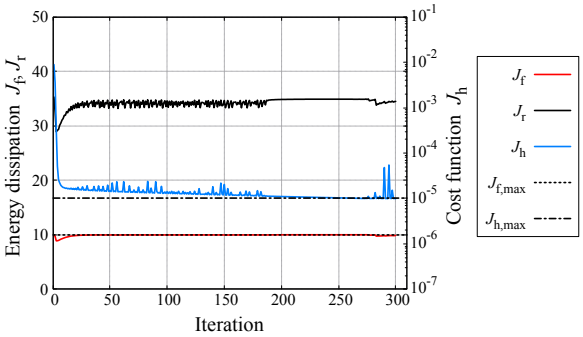

Fig. 21: Optimization history of the result with the geometric constraint in full-scale 3D case

Fig. 22: Fictitious physical field of obtained solution with the geometric constraint $J_{\mathrm{h,max}} = 1 \times 10^{-5}$

Appendix A Expressions of the energy dissipation

In this section, we describe the conservation of the mechanical energy of the Newtonian fluid in the control volume Ω shown in Fig. A.1. Similar explanations can be seen in [Lin et al., 2015]. The governing equations of a steady-state incompressible flow with Brinkman penalization are described as follows:

$$\begin{cases} -\nabla\cdot\left(\boldsymbol{u}\boldsymbol{u}^{\top}\right)-\nabla p+\nabla\cdot\bar{\boldsymbol{\tau}}-\alpha\boldsymbol{u}=\boldsymbol{0} & \text{in } \Omega \\ \nabla\cdot\boldsymbol{u}=0 & \text{in } \Omega, \end{cases} \tag{A.1}$$

where $\bar{\boldsymbol{\tau}}$ denotes the viscous stress tensor defined as,

$$\bar{\boldsymbol{\tau}} := \frac{1}{\mathrm{Re}}\left(\nabla\boldsymbol{u}+\nabla\boldsymbol{u}^{\top}\right). \tag{A.2}$$

Multiplying the momentum equation by the velocity $\boldsymbol{u}$ as inner product yields, after some manipulations,

$$\nabla\cdot\left\{-\left(p+\frac{\boldsymbol{u}^2}{2}\right)\boldsymbol{u}\right\}+\nabla\cdot\boldsymbol{\tau}=\Phi+\alpha\boldsymbol{u}^2, \tag{A.3}$$

where $\boldsymbol{\tau} := \bar{\boldsymbol{\tau}}\cdot\boldsymbol{n}$, and Φ is the dissipation function defined as,

$$\Phi := \bar{\boldsymbol{\tau}}\colon\nabla\boldsymbol{u}=\frac{1}{2\mathrm{Re}}\left(\nabla\boldsymbol{u}+\nabla\boldsymbol{u}^{\top}\right)^2. \tag{A.4}$$

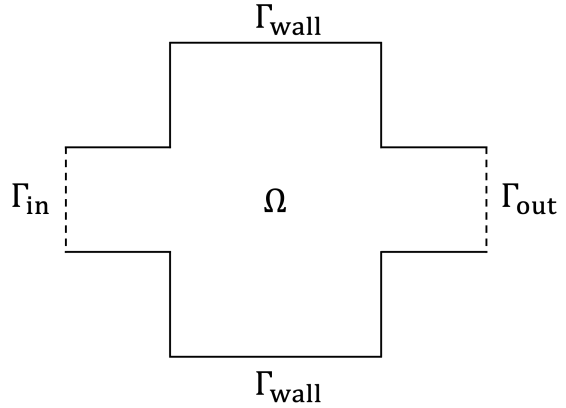

Fig. A.1: Control volume Ω for considering energy conservation

Taking the domain integral of (A.3) and applying the divergence theorem yields the following relation.

$$\begin{aligned} &-\int_{\Gamma}\left(p+\frac{\boldsymbol{u}^2}{2}\right)(\boldsymbol{u}\cdot\boldsymbol{n})\,\mathrm{d}\Gamma+\int_{\Gamma}\boldsymbol{\tau}\cdot\boldsymbol{u}\mathrm{d}\Gamma \\ &=\int_{\Omega}\left(\Phi+\alpha\boldsymbol{u}^2\right)\mathrm{d}\Omega. \end{aligned} \tag{A.5}$$

The boundary $\Gamma=\partial\Omega$ of the control volume Ω consists of inlet Γ_{in}, outlet Γ_{out} and wall Γ_{wall}. On the wall Γ_{wall}, the velocity is equal to zero.

$$\boldsymbol{u}=\boldsymbol{0} \text{ on } \Gamma_{\mathrm{wall}}. \tag{A.6}$$

Therefore, the equation (A.5) can be transformed to:

$$\begin{aligned} &-\int_{\Gamma_{\mathrm{in}}\cup\Gamma_{\mathrm{out}}}\left(p+\frac{\boldsymbol{u}^2}{2}\right)(\boldsymbol{u}\cdot\boldsymbol{n})\,\mathrm{d}\Gamma+\int_{\Gamma_{\mathrm{in}}\cup\Gamma_{\mathrm{out}}}\boldsymbol{\tau}\cdot\boldsymbol{u}\mathrm{d}\Gamma \\ &=\int_{\Omega}\left(\Phi+\alpha\boldsymbol{u}^2\right)\mathrm{d}\Omega. \end{aligned} \tag{A.7}$$

The second term in the left-hand side of (A.7) implies work done by viscous stress on the inlet and outlet boundaries. Although it can be considered as negligible in general, this term can be also theoretically neglected if fully developed flow is assumed. Then, the following relation is obtained.

$$-\int_{\Gamma_{\mathrm{in}}\cup\Gamma_{\mathrm{out}}}\left(p+\frac{\boldsymbol{u}^2}{2}\right)(\boldsymbol{u}\cdot\boldsymbol{n})\,\mathrm{d}\Gamma=\int_{\Omega}\left(\Phi+\alpha\boldsymbol{u}^2\right)\mathrm{d}\Omega. \tag{A.8}$$

Here, we have two equivalent expressions of energy dissipation. Therefore, the definition of diodicity Di' in the previous works [Lin et al., 2015, Sato et al., 2017a] and the definition in this work (15) are equivalent. Additionally, if the shapes of the inlet and the outlet are identical, the fully developed velocity profiles on the inlet and the outlet are the same, and thus the total flux of the kinematic energies is equal to zero:

$$\int_{\Gamma_{\mathrm{in}}}\frac{\boldsymbol{u}^2}{2}(\boldsymbol{u}\cdot\boldsymbol{n})\,\mathrm{d}\Gamma+\int_{\Gamma_{\mathrm{out}}}\frac{\boldsymbol{u}^2}{2}(\boldsymbol{u}\cdot\boldsymbol{n})\,\mathrm{d}\Gamma=0 \tag{A.9}$$

Therefore, the left-hand side of (A.8) can be rewritten as,

$$\begin{aligned} &-\int_{\Gamma_{\text{in}}\cup\Gamma_{\text{out}}} \left(p+\frac{\boldsymbol{u}^2}{2}\right)(\boldsymbol{u}\cdot\boldsymbol{n})\,\mathrm{d}\Gamma \\ &=-\int_{\Gamma_{\text{in}}\cup\Gamma_{\text{out}}} p\,(\boldsymbol{u}\cdot\boldsymbol{n})\,\mathrm{d}\Gamma \\ &=(p_{\text{in}}-p_{\text{out}})\cdot Q=\Delta p\cdot Q, \end{aligned} \tag{A.10}$$

where Δp is the static pressure drop and $Q := \int_{\Gamma_{\text{in}}}(-\boldsymbol{u}\cdot\boldsymbol{n})\,\mathrm{d}\Gamma = \int_{\Gamma_{\text{out}}}\boldsymbol{u}\cdot\boldsymbol{n}\mathrm{d}\Gamma$ is the flow rate. Thus, from equations (14) and (15), the two expressions of diodicity Di and Di$'$ are equivalent.

Appendix B Sensitivity analysis

In this section, the derivation of adjoint systems and sensitivities are briefly described. For simplicity, we use the following expressions of the governing equations in the residual form.

$$\begin{cases} \boldsymbol{R}_u(\boldsymbol{u},p,\gamma) \\ \quad=\nabla\cdot\left(\boldsymbol{u}\boldsymbol{u}^\top\right)-\nabla\cdot\bar{\boldsymbol{\sigma}}\,(\boldsymbol{u},p)+\alpha(\gamma)\boldsymbol{u}=\boldsymbol{0} \\ R_p(\boldsymbol{u},\gamma)=-\nabla\cdot\boldsymbol{u}=0 \\ R_T(T,\gamma) \\ \quad=\nabla\cdot(d(\gamma)\nabla T)+(1-\hat{\gamma}-T)=0. \end{cases} \tag{B.1}$$

The extended objective function $\mathcal{J}(\boldsymbol{u}_{\text{r}},p_{\text{r}},\gamma)$ and constraint functions $\mathcal{G}_1(\boldsymbol{u}_{\text{f}},p_{\text{f}},\gamma)$ and $\mathcal{G}_2(\boldsymbol{u}_{\text{f}},p_{\text{f}},\gamma)$ are defined as follows:

$$\begin{aligned} \mathcal{J}(\boldsymbol{u}_{\text{r}},p_{\text{r}},\gamma) &= J(\boldsymbol{u}_{\text{r}},p_{\text{r}}) \\ &\quad+\int_\Omega(-\boldsymbol{R}_u(\boldsymbol{u}_{\text{r}},p_{\text{r}},\gamma))\cdot\boldsymbol{u}_{\text{r}}{}'\mathrm{d}\Omega \\ &\quad+\int_\Omega(-R_p(\boldsymbol{u}_{\text{r}},\gamma))\,p_{\text{r}}'\mathrm{d}\Omega \\ \mathcal{G}_1(\boldsymbol{u}_{\text{f}},p_{\text{f}},\gamma) &= G_1(\boldsymbol{u}_{\text{f}},p_{\text{f}}) \\ &\quad+\int_\Omega\boldsymbol{R}_u(\boldsymbol{u}_{\text{f}},p_{\text{f}},\gamma)\cdot\boldsymbol{u}_{\text{f}}{}'\mathrm{d}\Omega \\ &\quad+\int_\Omega R_p(\boldsymbol{u}_{\text{f}},\gamma)p_{\text{f}}'\mathrm{d}\Omega \\ \mathcal{G}_2(T,\gamma) &= G_2(T,\gamma) \\ &\quad+\int_\Omega R_T(T,\gamma)T'\mathrm{d}\Omega \end{aligned} \tag{B.2}$$

where $\boldsymbol{u}_{\text{f}}{}'$ and p_{f}' are adjoint variables for the forward flow, $\boldsymbol{u}_{\text{r}}{}'$ and p_{r}' are adjoint variables for the reverse flow, and T' is the adjoint variable for the fictitious physical field. The residuals are multiplied by -1 in the definition of $\mathcal{J}$ for simplicity of the following derivation.

The adjoint equations are derived from the conditions that partial variations of the extended objective and constraint functions with respect to the state variables are zero. The resultant adjoint systems are described as follows:

$$\begin{cases} -\left(\nabla\boldsymbol{u}_{\text{r}}{}'+\nabla\boldsymbol{u}_{\text{r}}{}'^\top\right)\cdot\boldsymbol{u}_{\text{r}} \\ \quad-\nabla\cdot\bar{\boldsymbol{\sigma}}\,(\boldsymbol{u}_{\text{r}}{}',p_{\text{r}}')+\alpha(\hat{\gamma})\boldsymbol{u}_{\text{r}}{}'=\boldsymbol{0} & \text{in } \Omega \\ \nabla\cdot\boldsymbol{u}_{\text{r}}{}'=0 & \text{in } \Omega \\ \boldsymbol{u}_{\text{r}}{}'=\boldsymbol{u}_D & \text{on } \Gamma_D \\ \bar{\boldsymbol{\sigma}}\,(\boldsymbol{u}_{\text{r}}{}',p_{\text{r}}')\cdot\boldsymbol{n} \\ =\dfrac{\boldsymbol{u}_{\text{r}}{}^2}{2}+(\boldsymbol{u}_{\text{r}}\cdot\boldsymbol{n})\,\boldsymbol{u}_{\text{r}} \\ \quad-(\boldsymbol{u}_{\text{r}}\cdot\boldsymbol{n})\,\boldsymbol{u}_{\text{r}}{}'-(\boldsymbol{u}_{\text{r}}\cdot\boldsymbol{u}_{\text{r}}{}')\,\boldsymbol{n} & \text{on } \Gamma_N, \end{cases} \tag{B.3}$$

$$\begin{cases} -\left(\nabla\boldsymbol{u}_{\text{f}}{}'+\nabla\boldsymbol{u}_{\text{f}}{}'^\top\right)\cdot\boldsymbol{u}_{\text{f}} \\ \quad-\nabla\cdot\bar{\boldsymbol{\sigma}}\,(\boldsymbol{u}_{\text{f}}{}',p_{\text{f}}')+\alpha(\hat{\gamma})\boldsymbol{u}_{\text{f}}{}'=\boldsymbol{0} & \text{in } \Omega \\ \nabla\cdot\boldsymbol{u}_{\text{f}}{}'=0 & \text{in } \Omega \\ \boldsymbol{u}_{\text{f}}{}'=\boldsymbol{u}_D & \text{on } \Gamma_D \\ \bar{\boldsymbol{\sigma}}\,(\boldsymbol{u}_{\text{f}}{}',p_{\text{f}}')\cdot\boldsymbol{n} \\ =\dfrac{\boldsymbol{u}_{\text{f}}{}^2}{2}+(\boldsymbol{u}_{\text{f}}\cdot\boldsymbol{n})\,\boldsymbol{u}_{\text{f}} \\ \quad-(\boldsymbol{u}_{\text{f}}\cdot\boldsymbol{n})\,\boldsymbol{u}_{\text{f}}{}'-(\boldsymbol{u}_{\text{f}}\cdot\boldsymbol{u}_{\text{f}}{}')\,\boldsymbol{n} & \text{on } \Gamma_N, \end{cases} \tag{B.4}$$

$$\begin{cases} \nabla\cdot(d\,(\hat{\gamma})\,\nabla T')-T'+2\,(1-\hat{\gamma})\,T=0 & \text{in } \Omega \\ T'=0 & \text{on } \Gamma_T \\ d\nabla T'\cdot\boldsymbol{n}=0 & \text{on } \Gamma_q. \end{cases} \tag{B.5}$$

The sensitivity of the objective function J with respect to the design variable γ can be described as follows:

$$\frac{\delta\mathcal{J}}{\delta\gamma}=\frac{\delta\mathcal{J}}{\delta\hat{\gamma}}\frac{\partial\hat{\gamma}}{\partial\tilde{\gamma}}\frac{\delta\tilde{\gamma}}{\delta\gamma}, \tag{B.6}$$

where the functional derivative of $\mathcal{J}$ with respect to the projected density $\hat{\gamma}$ is derived as:

$$\frac{\delta\mathcal{J}}{\delta\hat{\gamma}}=-\frac{\partial\alpha}{\partial\hat{\gamma}}\,(\boldsymbol{u}_{\text{r}}\cdot\boldsymbol{u}_{\text{r}}{}')=\alpha_{\max}\,(\boldsymbol{u}_{\text{r}}\cdot\boldsymbol{u}_{\text{r}}{}')\ \text{ in } \Omega, \tag{B.7}$$

and the term $\dfrac{\partial\hat{\gamma}}{\partial\tilde{\gamma}}$ is the derivative of the smoothed Heaviside function (6) with respect to the filtered density $\tilde{\gamma}$:

$$\frac{\partial\hat{\gamma}}{\partial\tilde{\gamma}}=\frac{\beta\left(1-\tanh^2(\beta(\tilde{\gamma}-\eta))\right)}{\tanh(\beta\eta)+\tanh(\beta(1-\eta))}. \tag{B.8}$$

Then, the functional derivative of $\mathcal{J}$ with respect to the design variable γ is obtained as the solution of the adjoint Helmholtz-type partial differential equation, that is:

$$\begin{cases} -r^2\nabla^2 S_{\mathcal{J}} + S_{\mathcal{J}} = S_{\mathcal{J},\tilde{\gamma}} & \text{in } \Omega \\ \nabla S_{\mathcal{J}} \cdot \boldsymbol{n} = 0 & \text{on } \Gamma, \end{cases} \tag{B.9}$$

where,

$$S_{\mathcal{J}} := \frac{\delta \mathcal{J}}{\delta \gamma}, \quad S_{\mathcal{J},\tilde{\gamma}} := \frac{\delta \mathcal{J}}{\delta \hat{\gamma}} \frac{\partial \hat{\gamma}}{\partial \tilde{\gamma}}. \tag{B.10}$$

In the same manner, the sensitivities of constraint functions G_1 and G_2 with respect to the design variable γ can be derived by replacing $\mathcal{J}$ in the above process with $\mathcal{G}_1$ and $\mathcal{G}_2$. The resultant functional derivatives of $\mathcal{G}_1$ and $\mathcal{G}_2$ with respect to the projected density $\hat{\gamma}$ are described as:

$$\begin{aligned} \frac{\delta \mathcal{G}_1}{\delta \hat{\gamma}} &= \frac{\partial \alpha}{\partial \hat{\gamma}} \left(\boldsymbol{u}_{\mathrm{f}} \cdot \boldsymbol{u}_{\mathrm{f}}{}' \right) = -\alpha_{\max} \left(\boldsymbol{u}_{\mathrm{f}} \cdot \boldsymbol{u}_{\mathrm{f}}{}' \right) \text{ in } \Omega, \\ \frac{\delta \mathcal{G}_2}{\delta \hat{\gamma}} &= -\frac{\partial d}{\partial \hat{\gamma}} \left(\nabla T \cdot \nabla T' \right) - T' - T^2 \\ &= \left(d_{\max} - d_{\min} \right) \left(\nabla T \cdot \nabla T' \right) - T' - T^2 \text{ in } \Omega. \end{aligned} \tag{B.11}$$

Appendix C Fictitious physical model formulation

In the previous work [Yamada and Noguchi, 2022], the governing equation for the fictitious physical field is given as follows:

$$\begin{cases} \nabla \cdot \left(d\left(\hat{\gamma}\right) \nabla T \right) + \left(1 - \hat{\gamma}\right)\left(1 - T\right) = 0 & \text{in } \Omega \\ T = 0 & \text{on } \Gamma_T \\ d \nabla T \cdot \boldsymbol{n} = 0 & \text{on } \Gamma_q, \end{cases} \tag{C.1}$$

The difference is in the definition of the heat source,

$$Q(\hat{\gamma}, T) = \begin{cases} \left(1 - \hat{\gamma} - T\right) := Q_1(\hat{\gamma}, T) \\ \left(1 - \hat{\gamma}\right)\left(1 - T\right) := Q_2(\hat{\gamma}, T), \end{cases} \tag{C.2}$$

where $Q_1(\hat{\gamma}, T)$ is used in this work and $Q_2(\hat{\gamma}, T)$ is used in the previous work.

Fig. C.1 shows the fictitious physical field when the governing equation (C.1) is used for the same problem setting in Section 4.1. In this case, it seems that $d_{\max} = 1 \times 10^1$ and $d_{\min} \leq 1 \times 10^{-5}$ are the appropriate values for the diffusion coefficients. As mentioned in [Yamada and Noguchi, 2022], $T \approx 1$ in the "floating" islands (or, closed cavities in [Yamada and Noguchi, 2022]) is achieved regardless of their size.

However, in the fluid domain (or the material domain) $\hat{\gamma} = 1$, the fictitious temperature T has non-zero value especially near the "floating" islands, which may lead to undesirable effects on the optimization process. This behavior may have not become an important issue in the previous work because the target of penalization was the void cavities in the mean compliance minimization problem and the thermal diffusivity problem, where the material domains $\hat{\gamma} = 1$ are usually surrounded by the void domains $\hat{\gamma} = 0$. In the fluid problems, however, it is often the case that the fluid domains occupy most of the design domain, especially in the case without volume constraint. Therefore, the fictitious physical field governed by (C.1) might not work as expected, and we employed another expression $Q_1(\hat{\gamma}, T)$ in (C.2) for the heat source $Q(\hat{\gamma}, T)$ in this paper.

Supplementary Information

No supplementary information is used in this paper.

Acknowledgement

No funding was received for conducting this study.

Declarations

Conflict of interest

On behalf of all authors, the corresponding author states that there is no conflict of interest.

Replication of results

The presented results were obtained using OpenFOAM and we can provide them upon reasonable request.

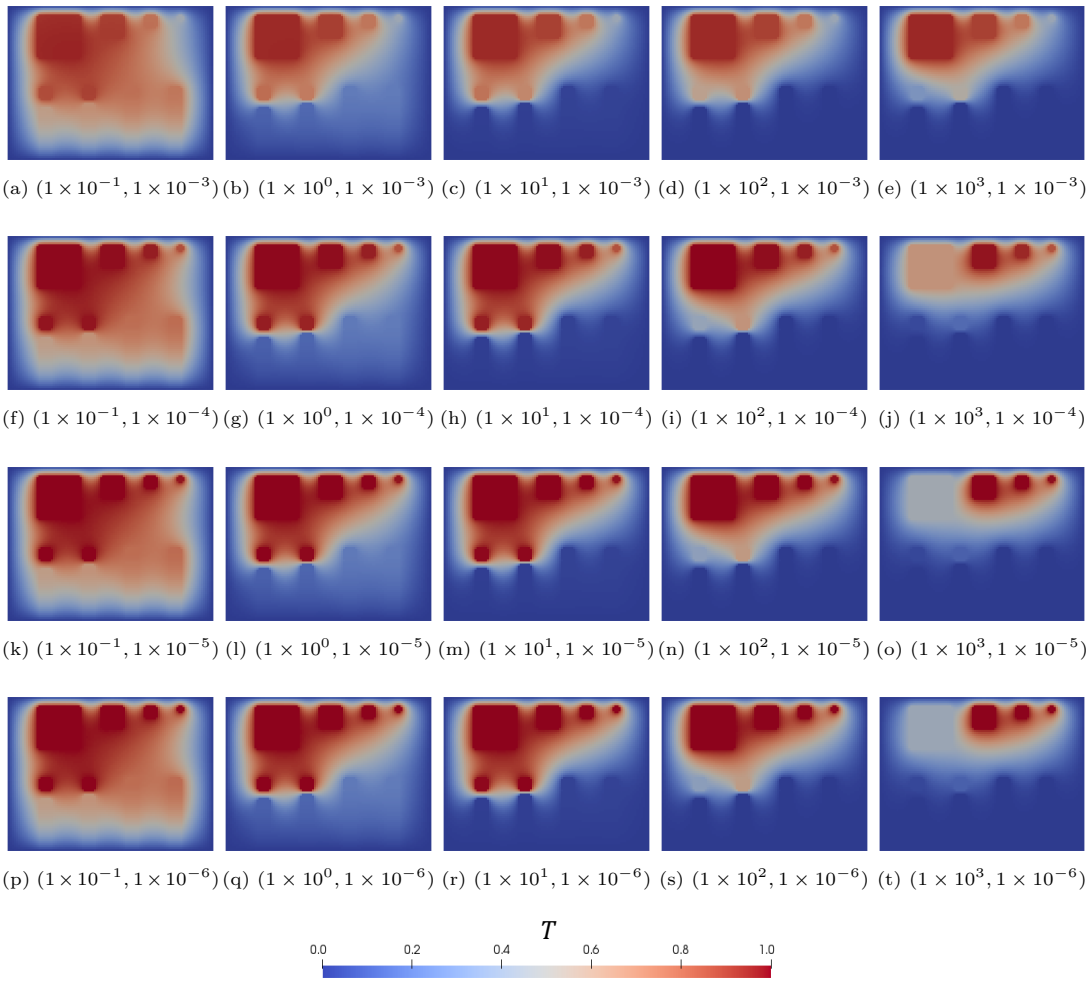

Fig. C.1: Fictitious physical field T in the work by Yamada and Noguchi [2022] for various diffusion coefficients $(d_{\max}, d_{\min})$

References

G. Allaire, F. Jouve, and G. Michailidis. Molding direction constraints in structural optimization via a level-set method. *Variational Analysis and Aerospace Engineering: Mathematical Challenges for the Aerospace of the Future*, pages 1–39, 2016.

M. P. Bendsøe and N. Kikuchi. Generating optimal topologies in structural design using a homogenization method. *Computer Methods in Applied Mechanics and Engineering*, 71(2): 197–224, 1988. ISSN 0045-7825.

T. Borrvall and J. Petersson. Topology optimization of fluids in stokes flow. *International Journal for Numerical Methods in Fluids*, 41(1): 77–107, 2003.

Y. Deng, Z. Liu, P. Zhang, Y. Wu, and J. G. Korvink. Optimization of no-moving part fluidic resistance microvalves with low reynolds number. In *2010 IEEE 23rd International conference on micro electro mechanical systems (MEMS)*, pages 67–70. IEEE, 2010.

Y. Deng, Z. Liu, P. Zhang, Y. Liu, and Y. Wu. Topology optimization of unsteady incompressible navier–stokes flows. *Journal of Computational Physics*, 230(17):6688–6708, 2011.

C. B. Dilgen, S. B. Dilgen, D. R. Fuhrman, O. Sigmund, and B. S. Lazarov. Topology optimization of turbulent flows. *Computer Methods*

in Applied Mechanics and Engineering, 331: 363–393, 2018.

F. K. Forster, R. L. Bardell, M. A. Afromowitz, N. R. Sharma, and A. Blanchard. Design, fabrication and testing of fixed-valve micro-pumps. *Asme-Publications-Fed*, 234:39–44, 1995.

N. Galanos, E. M. Papoutsis-Kiachagias, K. C. Giannakoglou, Y. Kondo, and K. Tanimoto. Synergistic use of adjoint-based topology and shape optimization for the design of bi-fluid heat exchangers. *Structural and Multidisciplinary Optimization*, 65(9):245, 2022.

A. R. Gamboa, C. J. Morris, and F. K. Forster. Improvements in fixed-valve micropump performance through shape optimization of valves. *J. Fluids Eng.*, 127(2):339–346, 2005.

A. Gersborg-Hansen, O. Sigmund, and R. B. Haber. Topology optimization of channel flow problems. *Structural and Multidisciplinary Optimization*, 30(3):181–192, 2005.

A. Ghasemi and A. Elham. Efficient multi-stage aerodynamic topology optimization using an operator-based analytical differentiation. *Structural and Multidisciplinary Optimization*, 65(4): 130, 2022.

J. K. Guest. Imposing maximum length scale in topology optimization. *Structural and Multidisciplinary Optimization*, 37:463–473, 2009.

J. K. Guest, J. H. Prévost, and T. Belytschko. Achieving minimum length scale in topology optimization using nodal design variables and projection functions. *International Journal for Numerical Methods in Engineering*, 61(2): 238–254, 2004.

Y. Guo, H. Pan, E. Wadbro, and Z. Liu. Design applicable 3d microfluidic functional units using 2d topology optimization with length scale constraints. *Micromachines*, 11(6):613, 2020.

A. Kawamoto, T. Matsumori, S. Yamasaki, T. Nomura, T. Kondoh, and S. Nishiwaki. Heaviside projection based topology optimization by a pde-filtered scalar function. *Structural and Multidisciplinary Optimization*, 44(1): 19–24, 2011.

E. Kontoleontos, E. Papoutsis-Kiachagias, A. Zymaris, D. Papadimitriou, and K. Giannakoglou. Adjoint-based constrained topology optimization for viscous flows, including heat transfer. *Engineering Optimization*, 45(8): 941–961, 2013.

S. Kreissl, G. Pingen, and K. Maute. Topology optimization for unsteady flow. *International Journal for Numerical Methods in Engineering*, 87(13):1229–1253, 2011.

B. S. Lazarov and O. Sigmund. Filters in topology optimization based on helmholtz-type differential equations. *International Journal for Numerical Methods in Engineering*, 86(6): 765–781, 2011.

H. Li, T. Kondoh, P. Jolivet, K. Furuta, T. Yamada, B. Zhu, H. Zhang, K. Izui, and S. Nishiwaki. Optimum design and thermal modeling for 2d and 3d natural convection problems incorporating level set-based topology optimization with body-fitted mesh. *International Journal for Numerical Methods in Engineering*, 123(9):1954–1990, 2022a.

H. Li, T. Kondoh, P. Jolivet, N. Nakayama, K. Furuta, H. Zhang, B. Zhu, K. Izui, and S. Nishiwaki. Topology optimization for lift–drag problems incorporated with distributed unstructured mesh adaptation. *Structural and Multidisciplinary Optimization*, 65(8):1–15, 2022b.

H. Li, M. Yu, P. Jolivet, J. Alexandersen, T. Kondoh, T. Hu, K. Furuta, K. Izui, and S. Nishiwaki. Reaction–diffusion equation driven topology optimization of high-resolution and feature-rich structures using unstructured meshes. *Advances in Engineering Software*, 180:103457, 2023.

Q. Li, W. Chen, S. Liu, and L. Tong. Structural topology optimization considering connectivity constraint. *Structural and Multidisciplinary Optimization*, 54:971–984, 2016.

S. Lin, L. Zhao, J. K. Guest, T. P. Weihs, and Z. Liu. Topology optimization of fixed-geometry fluid diodes. *Journal of Mechanical Design*, 137(8):081402, 2015.

S. Liu, Q. Li, W. Chen, L. Tong, and G. Cheng. An identification method for enclosed voids restriction in manufacturability design for additive manufacturing structures. *Frontiers of Mechanical Engineering*, 10:126–137, 2015.

E. Morganti, G. Pignatel, et al. Microfluidics for the treatment of the hydrocephalus. In *Proceedings of International Conference on Sensing Technology, Palmerston North*, pages 483–487, 2005.

M. Nabavi. Steady and unsteady flow analysis in microdiffusers and micropumps: a critical review. *Microfluidics and Nanofluidics*, 7: 599–619, 2009.

L. H. Olesen, F. Okkels, and H. Bruus. A high-level programming-language implementation of topology optimization applied to steady-state Navier–Stokes flow. *International Journal for Numerical Methods in Engineering*, 65(7): 975–1001, 2006.

C. Othmer. A continuous adjoint formulation for the computation of topological and surface sensitivities of ducted flows. *International Journal for Numerical Methods in Fluids*, 58(8): 861–877, 2008.

S. Pan, M. Yu, H. Li, Z. Li, M. Ren, J. Gu, and C. Shen. An integrated two-step strategy for an optimal design of liquid-cooled channel layout based on the mmc–density approach. *Structural and Multidisciplinary Optimization*, 65(8):221, 2022.

G. Pingen and K. Maute. Optimal design for non-newtonian flows using a topology optimization approach. *Computers & Mathematics with Applications*, 59(7):2340–2350, 2010.

T. A. Poulsen. A new scheme for imposing a minimum length scale in topology optimization. *International Journal for Numerical Methods in Engineering*, 57(6):741–760, 2003.

J. Romero and E. C. N. Silva. A topology optimization approach applied to laminar flow machine rotor design. *Computer Methods in Applied Mechanics and Engineering*, 279: 268–300, 2014.

Y. Sato, K. Yaji, K. Izui, T. Yamada, and S. Nishiwaki. Topology optimization of a no-moving-part valve incorporating pareto frontier exploration. *Structural and Multidisciplinary Optimization*, 56:839–851, 2017a.

Y. Sato, T. Yamada, K. Izui, and S. Nishiwaki. Manufacturability evaluation for molded parts using fictitious physical models, and its application in topology optimization. *The International Journal of Advanced Manufacturing Technology*, 92:1391–1409, 2017b.

K. Svanberg. The method of moving asymptotes—a new method for structural optimization. *International Journal for Numerical Methods in Engineering*, 24(2):359–373, 1987.

T. Truong and N. Nguyen. Simulation and optimization of tesla valves. *Nanotech*, 1:178–181, 2003.

F. Wang, B. S. Lazarov, and O. Sigmund. On projection methods, convergence and robust formulations in topology optimization. *Structural and Multidisciplinary Optimization*, 43: 767–784, 2011.

Q. Xia, T. Shi, M. Wang, and S. Liu. A level set based method for the optimization of cast part. *Structural and Multidisciplinary Optimization*, 41:735–747, 2010.

K. Yaji, T. Yamada, S. Kubo, K. Izui, and S. Nishiwaki. A topology optimization method for a coupled thermal–fluid problem using level set boundary expressions. *International Journal of Heat and Mass Transfer*, 81:878–888, 2015.

T. Yamada and Y. Noguchi. Topology optimization with a closed cavity exclusion constraint for additive manufacturing based on the fictitious physical model approach. *Additive Manufacturing*, 52:102630, 2022.

G. H. Yoon. Topology optimization for turbulent flow with spalart–allmaras model. *Computer Methods in Applied Mechanics and Engineering*, 303:288–311, 2016.

M. Yu, S. Ruan, J. Gu, M. Ren, Z. Li, X. Wang, and C. Shen. Three-dimensional topology optimization of thermal-fluid-structural problems for cooling system design. *Structural and Multidisciplinary Optimization*, 62:3347–3366, 2020.

M. Zhou, B. S. Lazarov, F. Wang, and O. Sigmund. Minimum length scale in topology optimization by geometric constraints. *Computer Methods in Applied Mechanics and Engineering*, 293:266–282, 2015.

S. Zhou and Q. Li. A variational level set method for the topology optimization of steady-state navier–stokes flow. *Journal of Computational Physics*, 227(24):10178–10195, 2008.